

1 A shallow earthquake swarm close to
2 hydrocarbon activities: discriminating
3 between natural and induced causes for
4 the 2018–19 Surrey, UK earthquake
5 sequence

6 Stephen P. Hicks¹, James Verdon², Brian Baptie³, Richard Lockett³, Zoë K. Mildon⁴, Thomas
7 Gernon⁵

8 1. Department of Earth Science and Engineering, Imperial College London, U.K.

9 2. School of Earth Sciences, University of Bristol, UK.

10 3. British Geological Survey, Edinburgh, UK.

11 4. School of Geography, Earth and Environmental Sciences, University of Plymouth, Plymouth, UK

12 5. School of Ocean and Earth Science, University of Southampton, U.K.

13 **Abstract**

14 Earthquakes induced by subsurface industrial activities are a globally emotive issue, with a
15 growing catalogue of induced earthquake sequences. However, attempts at discriminating
16 between natural and induced causes, particularly for anomalously shallow seismicity, can be
17 challenging. An earthquake swarm during 2018–19 in south-east England with a maximum
18 magnitude of M_L 3.2 received great public and media attention because of its proximity to
19 operating oilfields. It is therefore vital and timely to provide a detailed characterisation of the
20 earthquake sequence at present, and to decide based on current evidence, whether the
21 earthquakes were likely natural or induced. We detected 129 earthquakes and computed
22 detailed source parameters of these events. Most earthquakes occurred at a shallow depth of
23 2.3 km, >1 km deeper than the geological formations targeted by the oilfields, and laterally >3
24 km away from the drill-sites. We combine the east-west trending cluster of the seismicity with 2-
25 D seismic reflection profiles to find the causative fault system for the earthquakes. A b -value close
26 to unity and strike-slip faulting mechanisms are consistent with tectonic reactivation along a pre-
27 existing fault. Overall, we find no indicators in the earthquake parameters that would strongly
28 suggest an induced source. Nor do we find any clear trends between drilling activities and
29 seismicity based on operational logs provided by the operators. Injected volumes are near-zero
30 and monthly production amounts are many orders of magnitude smaller than other reported
31 cases of extraction-induced seismicity. On balance, and based on the available evidence, we find
32 it currently unlikely that nearby industrial activities induced the seismic swarm. Most likely, the
33 Surrey earthquakes offer a uniquely detailed insight into shallow seismicity within sedimentary

*This is a non-peer-reviewed pre-print submitted to Seismological Research Letters.
Findings are subject to change.*

34 basins. Nevertheless, the way that activity reporting by operators themselves is regulated
35 remains a controversial issue when discriminating between natural and induced seismicity for
36 industrial methods that have not been expected to induce earthquakes.

Non-peer reviewed pre-print

37 **Introduction**

38 In recent years, seismicity induced and triggered by industry has become a topic of great scientific
39 and public interest around the world. Seismic events near industrial facilities alarm local
40 communities yet discriminating between anthropogenic and natural seismicity is not a trivial task
41 (Grigoli *et al.*, 2017). Research has showed many forms of industrial activities can induce that
42 seismicity. These include: conventional hydrocarbon production (Segall, 1989), stimulating
43 geothermal reservoirs (Häring *et al.*, 2008), hydraulic fracturing (Clarke *et al.*, 2014), CO₂ storage
44 (Kaven *et al.*, 2015), coal mining (Wilson *et al.*, 2015), and wastewater injection (Keranen *et al.*,
45 2014). Induced seismicity has been observed to occur both within crystalline basement (Verdon,
46 2014) and the shallower sedimentary formations being targeted by these operations (Eaton *et*
47 *al.*, 2018). The poro-elastic response of shallow sedimentary rocks to changes in fluid pressure
48 over large distances is poorly understood (Goebel and Brodsky, 2018).

49 Conversely, anomalous seismic swarms occurring at shallow depth can have natural causes (e.g.
50 Bent *et al.*, 2017). Natural earthquakes close to industrial sites heighten public concern and can
51 cause financial loss to operating companies if mis-attributed as induced; an example being the
52 2015 M_w 6.1 Emilia, Italy earthquake (Dahm *et al.*, 2015; Grigoli *et al.*, 2017). Overall, the
53 mechanisms and occurrence statistics of very shallow earthquakes are poorly constrained.

54 Criteria to discriminate induced versus natural seismicity includes answering qualitative
55 questions (Davis and Frohlich, 1993; Verdon *et al.*, 2019), and more quantitative analyses such
56 as earthquake source studies, numerical modelling and statistical tests (Grigoli *et al.*, 2017).

57 The UK is one such area where induced earthquakes are a highly contentious issue. The
58 background seismicity rate is low, with the regional state of stress dominated by northwest-
59 southeast compression from the Mid-Atlantic Ridge and the Mediterranean (Baptie, 2010). Most
60 earthquakes occur in the north and west of mainland Britain (Figure 1). Anthropogenic
61 earthquakes in the UK account for ~20% of all earthquakes in the instrumental catalogue (Wilson
62 *et al.*, 2015). The greatest contributor has been coal mining (Kusznir *et al.*, 1980; Verdon *et al.*,
63 2018) in central-northern England, South Wales, and Scotland (Figure 1). The maximum observed
64 magnitude from coal mining induced seismicity is M_L 3.1 (Redmayne, 1988; Bishop *et al.*, 1993;
65 Wilson *et al.*, 2015). For geothermal induced seismicity, over 11,000 microseismic events were
66 detected during the Hot Dry Rock project in southwest England between 1982 and 1987 (Pine
67 and Batchelor, 2001). The largest event had a magnitude of M_L 2.0.

68 For hydrocarbon extraction, the largest induced event was the 2001 M_w 4.3 Ekofisk, North Sea
69 earthquake with water injection causing shallow slip in the overburden at <3 km depth
70 (Ottemöller *et al.*, 2005). In 2011, the first UK onshore hydraulic fracturing of shale took place
71 near Blackpool in northern England. Injection triggered an M_L 2.3 earthquake, ~1.8 km from the
72 Preese Hall-1 well, at 3.6 km depth (Clarke *et al.*, 2014). Hydraulic fracturing and induced
73 microseismicity resumed nearby in 2018 at Preston New Road, drawing public attention once
74 again to anthropogenic earthquakes (Clarke *et al.*, 2019, in review). Most past induced
75 earthquakes in the UK are small (M_L <3.1) and occur at shallow depth (<3 km). Therefore,
76 accurately characterising earthquake sources and understanding the causes of such weak near-
77 surface seismicity is challenging in areas with sparse seismic station coverage.

78 One such example is a sequence of small earthquakes that began on 1 April 2018, a few
79 kilometres from the villages of Newdigate and Charlwood in Surrey, UK (Figure 1, Figure 2). The
80 British Geological Survey (BGS) detected 32 small earthquakes between April 2018 and May 2019.
81 Nearby people in large settlements, such as Crawley, Dorking, and Gatwick Airport, felt many of
82 the earthquakes. Residents described shaking from the largest earthquake (M_L 3.2)
83 corresponding to a maximum intensity of 5 (*Strong* shaking) on the European Macroseismic Scale
84 (EMS); (Grünthal, 1998); (<http://earthquakes.bgs.ac.uk/research/SurreyEarthquakes.html>; last
85 accessed May 2019). The sequence attracted much public interest for several reasons. First,
86 south-east and southern England, which encompasses the Weald and Wessex basins, has a
87 relatively low background earthquake activity rate in comparison to other parts of Britain
88 (Musson and Sargeant, 2007). Few similar sequences have been recorded in the past (Figure 1).
89 Second, oilfield development and production activities at the active fields of Brockham and Horse
90 Hill lie within 10 km distance of the earthquake sequence (Figure 2). Whilst no operators in the
91 Weald have conducted, nor applied to do hydraulic fracturing, the UK's Traffic Light Scheme for
92 hydraulic fracturing-induced seismicity has received extensive media attention. 31 events in the
93 Newdigate swarm had magnitudes that exceed the current $M_L = 0.5$ "red light" threshold.
94 However, the nearest permanent station of the BGS national seismic network lies on the
95 southern coast of England, over 50 km away (Figure 1). This network sparsity made it difficult to
96 initially constrain depth and faulting mechanisms, which can help to discriminate between
97 natural and induced causes (Frohlich *et al.*, 2016). The strong macroseismic intensity

98 observations supported early shallow depth estimates (initially fixed to 5.0 km), raising further
99 suspicions over possible induced seismicity (Verdon *et al.*, 2019).

100 After the tenth recorded earthquake, we installed a network of five temporary broadband
101 seismometer stations in the epicentral region (Figure 2). Given the large interest in these
102 earthquakes, here we analyse available seismic data to make a coherent seismological analysis
103 of the 2018–19 Surrey earthquake sequence up to mid-May 2019. We interpret these events in
104 terms of the regional geological structure of the Weald Basin. We compare the spatial-temporal
105 evolution of the seismicity with reported activities associated with oilfield development and
106 production at the nearby Horse Hill and Brockham sites to understand its cause.

Non-peer reviewed pre-print

107 **Regional geological, industrial, and seismological context**

108 The epicentral area of the Newdigate sequence in the Weald Basin comprises uplifted
109 sedimentary rocks spanning south-east England, the eastern English Channel and northern
110 France (Figure 1). A wealth of 2-D seismic data from the UK Onshore Geophysical Library (UKOGL,
111 2019) allows for a robust characterisation of basin structure. The top Palaeozoic basement
112 beneath the centre of the Weald lies at 2,500–3,000 km depth (Butler and Pullan, 1990). An
113 interpreted regional seismic profile that runs ~20 km west of Newdigate shows sedimentary fill
114 extending to depths of >3,000 m in the basin centre (UKOGL, 2019). Oil drilling in the Weald has
115 targeted Jurassic rocks, including conventional reservoirs such as the Portland Sandstone, and
116 lower-permeability formations such as the Kimmeridge Clay (Andrews, 2014). The Mesozoic
117 basin sediments sit unconformably on Devonian-to-Lower Carboniferous Palaeozoic sedimentary
118 rocks, which have been deformed, but not metamorphosed, by the Variscan orogeny (Butler and
119 Pullan, 1990). Boreholes have rarely penetrated pre-Variscan units, and therefore are less well
120 studied.

121 The key structural features of the Weald Basin were originally formed during the Variscan
122 (Hansen *et al.*, 2002), generating east-west trending thrust faults. These were re-activated as
123 extensional faults during the Permian as post-orogenic collapse, forming the basin. We find large
124 extensional structures running through the Triassic and Jurassic sediments, rooted in the
125 underlying basement and preserving the original east-west trend, with most dipping to the south.

126 Angus Energy plc. operates the Brockham oilfield, ~8 km away from the earthquakes (Figure 2).
127 Brockham has produced relatively small volumes from the Portland Sandstone, with ~60,000 m³
128 gross water and oil since 2002. Produced formation water produced is re-injected back into the
129 reservoir. Overall, net output is greater than net injection. Production volumes since 2002 have
130 been in decline, with several pauses in operations over the years. The most recent pause in
131 operations occurred between February 2016 and March 2018. In 2017–2018, development work
132 from a side-track well targeted the deeper Kimmeridge Clay Formation.

133 Known colloquially as the “Gatwick Gusher”, the Horse Hill-1 (HH-1) development well lies ~3 km
134 away from the earthquake swarm (Figure 2). Operated by UK Oil & Gas plc. (UKOG), HH-1 was
135 first drilled in October 2014. UKOG first flow-tested the Portland Sandstone at ~600 m depth in
136 March 2016 and the Kimmeridge Shale at ~800 m depth in July 2018. To date, ~7,000 m³ of oil
137 has been produced at HH-1 since July 2018. According to the operator, no water is currently being
138 produced at the well, and no fluids are operationally injected into the reservoir.

139 Southern and south-east England is one of the least seismically active areas in the UK (Figure 1).
140 The largest instrumentally recorded event in the region was the M_L 4.3 earthquake in Folkestone
141 in 2009. The depth of this event was constrained by both teleseismic observations and regional
142 waveform modelling at 5 ± 2 km (Ottemöller *et al.*, 2009). There is also considerable evidence for
143 damaging earthquakes in the Dover Straits over the last 1000 years, for example an estimated
144 M_L 5.8 earthquake in 1580 (García-Moreno *et al.*, 2015). There are only a few recorded
145 earthquakes within the Weald Basin itself. In 2005, there were three small earthquakes near
146 Billingshurst (Figure 1, Label *a*), ~20 km west of the Newdigate sequence. The largest earthquake

147 of the Billingshurst sequence had a magnitude of M_L 2.1 and a shallow depth – likely less than 5–
148 10 km (Baptie and Luckett, 2018). Historical catalogues provide evidence for past earthquakes in
149 the Weald region over the last 500 years. For example, Musson (Musson, 2008) finds reports of
150 an earthquake on 5 May 1551. Although the limited macroseismic data means that a location
151 and magnitude cannot be determined, the reports suggest that it was strongly felt with an
152 intensity of 5 EMS in Dorking, ~8 km from the 2018–19 earthquake swarm. Further afield, there
153 were six earthquakes near Chichester on the south coast (Figure 1, Label *b*) in the 1800s with
154 estimated magnitudes of M_L 2.9–3.4 (Musson, 1994). Such earthquake sequences or swarms are
155 relatively common in Great Britain. Examples include Comrie, 1788–1801 and 1839–46 (Musson,
156 1993); Kintail, 1974 (Assumpção, 1981) Manchester, 2002–2003 (Baptie and Ottemoeller, 2003)
157 and Aberfoyle, 2003 (Ottemöller and Thomas, 2007). More recently, in 2014–2015 there was a
158 sequence of earthquakes near Oakham in the East Midlands of England. The three largest events
159 had magnitudes of 3.2, 3.5 and 3.8 M_L , with depths of less than 5 km.

160 None of the above sequences were linked to anthropogenic causes, although the Manchester
161 sequence occurred in a sedimentary basin where coal had been mined in the past.

162 **Data and methods**

163 Seismic waveform data for the first events comes mainly from the BGS national broadband
164 seismic network (Figure 1). In south-east England, there are several RaspberryShake (RS) stations
165 with geophone sensors (Anthony *et al.*, 2018), which improve the recording coverage of the
166 earthquakes (Figure 1). The closest RS station (AM.REC60) lies ~6 km from the epicentral region
167 of the swarm (Figure 2). After the first nine events, we installed a network of five temporary
168 stations in the area (Figure 2) comprising Güralp 3ESPC 30 s – 100 Hz seismometers, with a
169 sampling rate of 200 Hz. We installed two of these stations (GB.HORS and GB.RUSH) in mid-July
170 and three (GB.GATW, GB.STAN, GB.BRDL) in early August 2018 (Figure 3a). We analysed seismic
171 waveform data up until 13/05/2019 (see Data and Resources).

172 We derive our 1-D seismic velocity model from detailed sonic log information from nearby
173 boreholes (Note S1, Figure S1 & Table S1 in the electronic supplement to this article). To relocate
174 the earthquakes, we used NonLinLoc (Lomax *et al.*, 2009), which offers robust constraints on
175 location uncertainties compared with traditional single-event location codes. To assess any
176 smaller-scale structure in the spatial-temporal evolution of the seismicity, we also computed
177 double-difference relocations (Waldhauser and Ellsworth, 2000); (Note S1 in the electronic
178 supplement to this article). ~19,000 delay time pairs each for P- and S-waves and ~15,000 and
179 ~18,000 cross-correlation times for P- and S-waves, respectively, were selected for the double-
180 difference relocation. We computed magnitudes using the UK local magnitude (M_L) scale of
181 Lockett *et al.* (2019), suitable for near-field observations (Note S2 in the electronic supplement
182 to this article).

183 To detect further low-magnitude seismicity not in the initial BGS catalogue, we took two
184 approaches. (1) We used the Lassie software (Heimann, 2016), a stack-and-delay-based
185 coherence detector, to find and locate events using continuous data from the temporary seismic
186 network. Coherency is mapped using a smooth characteristic function calculated from
187 normalised waveform envelopes. From this catalogue, we then (2) ran a cross-correlation
188 template-matching algorithm on data from local stations. For this, we used 1.0 s-long template
189 waveforms incorporating P- and S-waves from the events in the catalogue. We utilised
190 EQcorrscan (Chamberlain *et al.*, 2018) to scan for earthquakes on data filtered at 5–15 Hz.
191 Detections were made when the network-stacked cross-correlation sum exceeds nine times the
192 median absolute deviation. We then manually re-picked and relocated positive detections. For
193 nearby RS station AM.REC60, we also scanned continuous waveforms before the first known
194 earthquake, extending back as far as September 2017, when this station was first installed. There
195 were no earlier positive detections; therefore, no significantly large earthquake ($M_L > 1.5$) likely
196 occurred here before 01/04/2018, so the main sequence started then.

197 To investigate the causal mechanism of the Newdigate earthquakes, we computed moment
198 tensors from waveforms, Gutenberg-Richter b -values, stress drops from displacement spectra,
199 and static stress transfer (see Notes S3, S4 & S5 in the electronic supplement to this article).

200 **Results**

201 Besides the 34 events recorded in the BGS catalogue, we detected a further 95 micro-
202 earthquakes from 12/07/2018 onwards, forming an overall catalogue of 129 events (Figure 2,
203 Figure 3b; Table S2 in the electronic supplement to this article). Hypocentres for well-constrained
204 events recorded by five temporary monitoring stations have a mean depth of 2.3 km. Most
205 locations have formal epicentral and depth uncertainties of <200 m and <500 m, respectively.
206 These solutions are robust as they vary little when relocated in different velocity models, and
207 they had low root-mean-square arrival time residuals (<60 ms). Given the high waveform
208 similarity between large events (Figure 4), we fixed the depth of events before 12/08/2018 to 2.3
209 km (Note S1 in the electronic supplement to this article).
210 Overall, the best-constrained events illuminate a seismogenic patch ~2.5 km long and extending
211 over 1.3 km in depth (Figure 2). Most event epicentres in our full catalogue appear to cluster
212 along a roughly linear band, trending east-west. A few microseismic events were detected up to
213 2 km away to the north and east of the main cluster of seismicity. High-precision double-
214 difference relocations of 95 events confirm the strong east-west alignment of seismicity (Figure
215 S2 in the electronic supplement to this article).
216 The temporary stations captured six of the larger earthquakes ($M_L \geq 1.9$) in July 2018 and February
217 2019 (Figure 3a-b), allowing us to probe rupture mechanisms and depths (see Figure 5 for
218 examples). The best-constrained moment tensor solutions have centroid depths of 2.2 ± 0.2 km,
219 consistent with hypocentre depths (Figure S7 in the electronic supplement to this article) and
220 show the same strike-slip faulting mechanism. The west-east nodal plane corresponds to the

221 alignment of seismicity (Figure 2). The double-couple percentage is high (>75%). Analysis of 218
222 P-wave polarities from the wider catalogue suggest that most events had this same mechanism,
223 with little variability (Figure 5c).

224 In Figure 2, we examine whether this cluster of earthquakes correlates with pre-existing faults
225 identified from 2-D seismic profiles (Note S6 in the electronic supplement to this article). Faults
226 within the Mesozoic sediments are relatively easy to find, most of which strike east-west and dip
227 towards the south. We also find north-dipping and ENE–WSW trending faults. The Newdigate
228 Fault (NGF) is a prominent east-west striking, south-dipping fault system showing a normal sense
229 of offset, which extends across much of the study area. Most epicentres lie along the projected
230 surface trace of the NGF, consistent with the west-east nodal plane of the focal mechanisms,
231 suggesting slip occurred along this fault system (Figure 2, Figure 5). We can see this overall
232 relationship more clearly in the double-difference relocations (Figure S2 in the electronic
233 supplement to this article).

234 The Triassic lowermost basin fill and underlying Palaeozoic rocks appear to be more heavily
235 faulted (Figure 6). Given the spacing of the 2-D seismic lines and the number of fault traces, we
236 have not attempted to map every fault in the lower units. However, we can assume that these
237 faults have similar trends and positions as the extensional faults that extend above them. The
238 double-difference locations show that most events occurred within the footwall of the NGF; they
239 likely occurred on a south-dipping fault at greater depth within the lowermost basin fill (Figure
240 6).

241 From fitting displacement spectra of earthquakes in the sequence (see Figure S3 in the electronic
242 supplement to this article for an example), we compute stress drops of 0.2–11.0 MPa (Figure S6
243 in the electronic supplement to this article). From modelled static stress changes resulting from
244 the $M_L > 2$ earthquakes, accounting for the depth and the fault geometry uncertainties, we find
245 that most events with $M_L > 2$ occurred in a region of positive static stress from earlier earthquakes
246 (Figure S8 in the electronic supplement to this article). For $M_L > 2$ earthquakes, we computed the
247 total accumulated static stress at the hypocentre before each earthquake (Table S3 in the
248 electronic supplement to this article) resolved onto fault geometries consistent with the
249 Newdigate and Horse Hill faults. For nearly all $M_L > 2$ earthquakes, changing the depth and/or
250 strike of the receiver faults within the range of uncertainties can cause positive stress changes.
251 For some earthquakes, the epicentres were too close, and therefore the static stress calculated
252 is unreliable (Steacy *et al.*, 2004).

253 We also assess the frequency-magnitude distribution of the Newdigate seismic sequence in
254 terms of the b -value of the Gutenberg-Richter relationship. We look at several timeframes for
255 this as the temporary local monitoring network was not in place for the start of the earthquake
256 sequence. We compute magnitude of completeness, M_c by minimising the residual between a
257 power law fit to the data and the observed distribution (Wiemer and Wyss, 2000). First, we
258 consider the entire earthquake sequence starting in April 2018. We find an M_c of ~ 2.2 , supported
259 by the overall M_c estimate for south-east England (Survey, 2010). Here, we find a best-fitting b -
260 value of 1.1 (Figure 7a).

261 For the time when the local temporary monitoring network was operational, we computed a
262 much lower M_c of -0.2. This is supported by the detection of few $M_L < 0.2$ events outside of the
263 hours of 1300 – 0500 (Figure S4 in the electronic supplement to this article) because of higher
264 daytime cultural noise. Previous studies (Staudenmaier *et al.*, 2018) show that the different
265 scaling between M_L and M_w for small earthquakes may cause an artificial bi-linear Gutenberg-
266 Richter fit. Therefore, we also used our spectral and moment tensor estimates of M_w to re-scale
267 the M_L values. For this part of the catalogue, we are still cannot include the larger magnitudes
268 with a single Gutenberg-Richter fit. We assume that this effect is due to M_c varying with time and
269 our relatively small catalogue of earthquakes under-sampling the true earthquake sequence with
270 an exponential distribution. In any case, we truncate the maximum magnitude at M_L 1.1. This
271 yields a b -value of 0.9 (Figure 7b).

Non-peer reviewed pre-print

272 **Discussion**

273 Based on the location of our interpreted subsurface faults and earthquake locations, we identify
274 the NGF zone as the causative structure for most of the earthquakes. Given this correlation, and
275 computed moment tensors, the earthquakes most likely represent right-lateral strike-slip faulting
276 along this west-east striking structure. In cross-section, the double-difference relocations imply
277 a steeply dipping fault plane (Figure 6, and Figure S2 in the electronic supplement to this article).
278 At the earthquake source depths, according to interpreted well logs from HH-1 and Brockham,
279 the rock types are mainly mudstone-rich Middle-Lower Jurassic to Upper Triassic sedimentary
280 rocks. The stronger limestone unit of the Penarth Formation at ~2.3 km depth could promote the
281 more brittle failure required for seismic slip.

282 There are few cases of very shallow (<3 km depth) earthquake sequences documented in the
283 literature, likely a result of sub-optimal station coverage needed to accurately resolve such
284 shallow depths. Many documented cases of shallow seismicity in stable continental regions
285 worldwide link such seismicity with induced causes, such as hydraulic fracturing (Clarke *et al.*,
286 2014; Eaton *et al.*, 2018), conventional oil production (Frohlich *et al.*, 2012), hydraulic fracturing
287 (Clarke *et al.*, 2014; Eaton *et al.*, 2018), and groundwater extraction (González *et al.*, 2012). There
288 are fewer documented cases of anomalously shallow natural earthquakes within sedimentary
289 basins, with most past cases confined to metamorphic (Maceira *et al.*, 2000; Bent *et al.*, 2017)
290 and igneous lithologies (Malone *et al.*, 1975). Most earthquakes in the UK are consistent with
291 rupture in the shallow to mid-crust, although many events have shallower, and often poorly
292 constrained depths. Earthquakes occurring at such depths are thought to be relatively rare in the

293 UK, with the most accurate depths for background seismicity lying between 5 and 15 km.
294 However, re-analysis of the 2005 Billingshurst sequence, 20 km to the west of Newdigate, has
295 suggested shallow event depths (Baptie and Luckett, 2018).

296 Given the location of the earthquakes, it is important to assess whether nearby oilfield activities
297 induced these events or whether they were natural. We first consider the problem within the
298 framework of the criteria established by Frohlich et al. (2016) since these were designed for both
299 injection- and extraction-based operations, without requiring knowledge of well pressures.

300 1. Past precedence. There are no known past earthquakes associated with oil and gas
301 activities in south-east England, also an area of low seismicity (Figure 1). The 2005
302 Billingshurst earthquakes in the Weald are the nearest analogue to the Newdigate events
303 as they occurred at a shallow depth but not close to any known hydrocarbon activities.
304 The long-term magnitude of completeness of the British Geological Survey seismicity
305 catalogue for the entire UK is likely $M_L \sim 3.0$ (Musson and Sargeant, 2007); therefore, we
306 cannot rule out smaller past earthquakes in the area. Induced seismicity has been
307 associated with hydraulic fracturing for shale gas in northern England (Clarke *et al.*, 2014)
308 and conventional hydrocarbon extraction in the North Sea (Ottemöller *et al.*, 2005;
309 Wilson *et al.*, 2015). Yet no documented cases exist of conventional onshore extraction
310 inducing seismicity on the British Isles. Compared to offshore plays, onshore reservoirs in
311 the UK typically produce hydrocarbons at much smaller volumes and rates.

312 2. Spatial correlation with industrial activities. Figure 1 shows that the Newdigate
313 earthquake cluster occurred 3–5 km away from HH-1 and 6–8 km from the Brockham site.

314 We find no events at closer distances to HH-1; nor do we find any systematic migration
315 of seismicity with time either away from or towards HH-1. The earthquakes are 1.0–1.5
316 km deeper than the Portland and Kimmeridge targets, which lie at 550–700 m and 700–
317 1000 m depth, respectively (Figure 6). The earthquakes also likely occurred within either
318 Triassic sedimentary rocks or the underlying deformed Palaeozoic rocks. Again, the linear
319 group of epicentres appear to line up along the mapped NGF (Figure 2).

320 3. Temporal links with industrial activities. Whilst oil licence sites lie close to the seismic
321 cluster, we also need to consider whether the earthquakes temporally correlate with
322 oilfield activities. Figure 3 shows a timeline of seismicity and nearby well operations. After
323 a two-year pause, production and associated injection activities resumed at the Brockham
324 site in March 2018, two weeks before the first earthquake on 01/04/2018. Therefore, a
325 coincidence exists between the start of the seismicity and the restart in activities at
326 Brockham. However, fluids have been produced at Brockham for 14 years previously
327 without inducing known seismicity. Nevertheless, induced seismicity has been shown to
328 often lag by many years the start of production in conventional, large hydrocarbon
329 reservoirs (Maury *et al.*, 1990). Work was carried out at HH-1 in March 2018 (Figure 3),
330 shortly before the first earthquake on 1 April. According to operator logs, this work
331 involved only preparing the site at the surface and no subsurface work in the borehole
332 took place. Flow testing at HH-1 in February–March 2016 and in July 2018 was a long time
333 both before and after the start of the earthquakes (Figure 3), so we find no direct
334 temporal correlation. Looking at events with magnitudes much greater than M_c , we find

335 that 30–50% of earthquakes in our catalogue occurred within 72 hours of a reported well
336 shut-in day at HH-1, whereas only 13–30% of events occurred during a period of oil
337 production (Figure 3). However, robustly determining any such correlation is uncertain. It
338 depends on the lower magnitude threshold chosen, and it is difficult to remove the effect
339 of aftershocks occurring very soon after mainshocks. For hydraulic fracturing and
340 wastewater injection, seismicity rates generally diminish during well shut-in periods
341 (Horton, 2012; Schultz *et al.*, 2016). For simultaneous extraction and injection, models
342 show that the highest pore pressure disturbance along basement faults may occur after
343 shut-in (Chang and Segall, 2016). For gas extraction, well shut-ins lead to an overall
344 decrease in earthquakes, although some critically stressed faults may rupture many years
345 later (Zbinden *et al.*, 2017).

346 Using the Frohlich *et al.* (2016) criteria, uncertainty arises from the testing the questions posed,
347 as we could classify the Newdigate sequence as either “Possibly Induced” or “Probably Induced”.
348 However, this approach is likely an over-simplification as it does not consider detailed source
349 parameters or knowledge of fluid pressure or pathways (Verdon *et al.*, 2019). We therefore
350 assess the seismic source parameters in whether they show an induced or natural cause for the
351 events. We then examine in more detail whether the oilfield activities conducted at HH-1 and
352 Brockham had the potential to induce earthquakes.

353 The faulting mechanisms (Figure 2, Figure 5) are similar to the overall pattern in the British Isles,
354 in which strike-slip faulting dominates (Fig. 1); (Baptie, 2010). The Newdigate earthquake focal
355 mechanisms are consistent with the regional stress field with the maximum horizontal stress

356 oriented northwest-southeast. None of our moment tensor solutions show a large non-double-
357 couple component (Figure 5), as is sometimes observed for induced earthquakes (Sileny, 2009;
358 Wang *et al.*, 2018). In cases where seismicity is induced by compaction in a conventional
359 reservoir, we expect normal faulting at the edges of the reservoir, and reverse faulting within the
360 overburden (Segall, 1989). Such mechanisms have been observed for compaction-induced events
361 at large, depleting hydrocarbon fields (Ottemöller *et al.*, 2005; Wees *et al.*, 2014; Dahm *et al.*,
362 2015; Willacy *et al.*, 2018). However, for the Newdigate events, the lack of such dip-slip
363 components in the computed focal mechanisms shows that a compaction/subsidence
364 mechanism did not cause the earthquakes. A faulting mechanism consistent with the regional
365 state of stress does not completely dictate a natural cause. Induced earthquakes because of fluid
366 injection or hydraulic fracturing also usually have a rupture geometry and sense-of-slip consistent
367 with regional stress directions (Clarke *et al.*, 2014; McNamara *et al.*, 2015). However, there has
368 been no large fluid injection at HH-1. Injection at Brockham is of produced water, with the volume
369 injected being smaller than the volume produced from the same formation (Figure 3), resulting
370 in net fluid withdrawal.

371 The mean stress drop of 3.2 MPa, given the uncertainty in corner frequency estimates, is
372 consistent with a wide range values computed for past earthquakes in Britain (Baptie *et al.*, 2005;
373 Ottemöller *et al.*, 2009). We can attribute the relatively low stress drop to the low shear strength
374 of sedimentary rocks (Ottemöller *et al.*, 2005). Debate continues on whether we can use stress
375 drop as an indicator of the events being induced. Hough (2014) suggests that induced
376 earthquakes may have stress drops up to ten times weaker than natural events of similar

377 magnitudes based on ground shaking intensity. However, Zhang et al. (2016) found no significant
378 stress drop variation between induced and natural earthquakes. Regardless, we find no evidence
379 for an abnormal stress drop for the Newdigate events.

380 The Gutenberg-Richter b -value can give insights into the underlying causes of earthquakes.
381 Seismicity caused by tectonic stresses on pre-existing faults usually has a b -value close to unity.
382 Conversely, seismicity induced by fluid-related processes, whether natural (Wyss *et al.*, 1997) or
383 because of fluid injection (Maxwell *et al.*, 2012), often has a higher b -value. The high magnitude
384 of completeness and relatively small size of our catalogue means that our computed b -value is
385 poorly constrained, but our best estimates suggest it is close to the global average of 1.0.
386 However, this does not on its own rule out a causal link with industrial activities, as many cases
387 of induced seismicity produce b -values close to 1. But overall this b -value suggests seismicity
388 controlled by tectonic stresses along a pre-existing fault, consistent with the imaged fault
389 structures (Figure 2, Figure 6).

390 In summary therefore, our observations of seismic source parameters are consistent with natural
391 tectonic earthquakes. Given the regional stress tensor, uncertainties in the style of faulting and
392 the static stress changes associated with the $M > 2$ earthquakes in this sequence, it is likely that
393 static stress triggering played a role (Figure S8 in the electronic supplement to this article). We
394 are not required to invoke fluid pressure changes, which have explained the spatial-temporal
395 evolution of injection-induced seismicity (Catalli *et al.*, 2013).

396 To our knowledge, seismicity caused by extraction has only been reported at very large
397 hydrocarbon fields where production has taken place for many years. In contrast, the relatively

398 small extraction volumes and rates at Brockham and HH-1 (Figure 3) likely do not promote
399 overburden failure. Compared to large oilfields globally, the Brockham reservoir is small, with
400 only ~60,000 m³ reported oil and water produced, with low rates of extraction, since 2002 (Figure
401 3). This volume is several orders of magnitude smaller than reservoirs where well-documented
402 production-induced seismicity has occurred (Segall, 1989). At Brockham, production over roughly
403 15 years has been balanced by re-injection of produced formation water back into the reservoir.
404 Also, the injection of produced water into a depleted reservoir from which oil has been extracted
405 is unlikely to increase the pressure in the reservoir to above pre-production levels, making
406 induced seismicity less likely (Rubinstein and Mahani, 2015). Overall, more fluid has been
407 extracted than withdrawn, so the net fluid balance is negative, and pore pressures in the
408 Brockham field are likely lower than when the reservoir was first produced from. As a result,
409 injection at Brockham can be ruled out as a cause. Many E-W and ENE–WSW striking faults
410 between Brockham and the Newdigate Fault (Figure 6) likely act as a baffle to fluids or hydraulic
411 pressure migrating towards the earthquake source region.

412 At HH-1, during the 2016 flow test, the operator injected approximately 50 m³ [in V1 as 150 m³,
413 which was – a typo] acid wash at a rate of 0.24 m³/min and pressure at the surface of 10 MPa. A
414 short-period of flow then followed this testing. Compared to well-studied cases of injection-
415 induced seismicity in the U.S. (Frohlich, 2012), these volumes and rates at HH-1 are much smaller.
416 Also, the flow testing that followed the acid injection would likely offset any transient pressure
417 increase. With a gap of over two years between acid wash at HH-1 and the first earthquake, a
418 mechanism involving a time lag of such duration is unlikely given the small volumes injected.

419 The earthquakes began in April 2018, pre-dating phase two of flow testing at HH-1 on 09/07/2018
420 (Figure 3). The second major cluster of earthquakes had also occurred by this time. Based on
421 available operational data, this eliminates HH-1 as a direct cause for these events.

422 The toe of the HH-1 well is close to the Horse Hill Fault but does not intersect it (Figure 2),
423 although we cannot estimate a fault damage zone width. Hypothetically, a structural connection
424 between the Horse Hill and Newdigate Faults could support this triggering mechanism by acting
425 as a conduit for fluid and pressure changes. Based on the available 2-D seismic profiles, although
426 we cannot completely rule out a diffuse fault transfer zone between the north-dipping Horse Hill
427 fault and south-dipping NGF, we find no clear evidence to suggest that these faults intersect at
428 depth.

429 The final possibility is that the first events of the seismic sequence were natural, but then flow
430 testing work at HH-1 subsequently induced a resumption of seismicity. If so, the only causative
431 mechanism would be one of extraction and pore pressure drawdown (Teufel *et al.*, 1991).
432 Induced seismicity at conventional hydrocarbon fields is typically produced by compaction and
433 slip within the overburden, which requires high production volumes from large, laterally
434 extensive fields. At HH-1, the volumes produced to date are small ($\sim 7,000 \text{ m}^3$), and oil has only
435 been produced for a very short time. We are not aware of any extraction-and-subsidence related
436 seismicity for such small fluid volumes reported in the scientific literature. As discussed above,
437 we would expect to have dip-slip motions associated with compaction, rather than the observed
438 strike-slip mechanisms. In such cases, we expect seismicity to occur within and above the zone
439 affected by pore pressure drawdown. For such volumes, this zone is unlikely to extend more than

*This is a non-peer-reviewed pre-print submitted to Seismological Research Letters.
Findings are subject to change.*

440 a few hundred metres from the well-bore; not 3 km away laterally and over 1 km below the
441 reservoir.

Non-peer reviewed pre-print

442 **Conclusions**

443 Based on the available evidence and consideration of possible triggering mechanisms, we
444 conclude that at present, it is unlikely that anthropogenic activities induced the 2018–2019
445 Newdigate seismic sequence. We draw this conclusion from the following key observations of
446 seismicity and hydrocarbon operations:

- 447 1. *Timing of the start of seismic activity.* Based on operators' logs, the earthquake sequence
448 started before subsurface activity and flow testing/production at HH-1 in 2018.
- 449 2. *Location.* The earthquakes occur at least 3 km from the nearest oilfield operations, which
450 would be an abnormally long distance for production-induced seismicity based on past
451 reported cases. The earthquakes did not occur directly above, within, or on the immediate
452 flanks of the extraction reservoir, which could show an induced cause (Segall and
453 Fitzgerald, 1998). We see no migration in the seismicity with time towards or away the oil
454 reservoirs.
- 455 3. *Temporal correlation with ongoing oilfield activities.* Based on detailed operational logs
456 provided by the operators, we find no clear link between seismicity rate and cumulative
457 oil production or activities at either HH-1 or Brockham. Some earthquakes occurred
458 during well shut-in periods at HH-1, however if this is a factor, the stress transfer
459 mechanism is unclear.
- 460 4. *Source mechanisms.* Highly double-couple strike-slip focal mechanisms are consistent
461 with the regional state of stress and background seismicity in the UK. We do not find dip-
462 slip faulting mechanisms that are observed for cases of production-induced seismicity

463 (Segall, 1989). The frequency-magnitude character of the seismicity is not abnormal and
464 shows a tectonic control on the earthquakes, consistent with reactivation of a pre-existing
465 fault. The presence of multiple faults imaged using 2-D seismic and double-difference
466 relocations can help to explain the swarm-like nature of the seismic sequence.

467 5. *Fluid volumes and stress.* The reported cumulative volumes of net production are many
468 orders of magnitude smaller than past reported cases of extraction-induced seismicity.
469 Therefore, for such volumes, we do not expect large-scale poro-elastic stress changes >10
470 MPa, which might be needed to induce seismicity (Segall, 1989). Aside from a small
471 volume injected for acid wash at HH-1 in 2016, long before the first earthquake, and small
472 volumes of fluid re-injection at Brockham that are exceeded by production volumes, the
473 volumes and rates involved are very small. These amounts are dwarfed by other reported
474 cases of fluid injection-induced seismicity over large distances (Goebel and Brodsky,
475 2018). Static stress modelling shows that earthquakes likely triggered each other by
476 loading multiple fault strands rather than any external driver of fluid pore pressure
477 changes.

478 6. *Fluid pathways.* There is no obvious connection between the Horse Hill and Newdigate
479 Faults which could plausibly offer a permeability pathway from HH-1 to the earthquakes.
480 Many west-east trending normal faults likely act as a baffle to fluid flow to/from
481 Brockham.

482 If all or some earthquakes were induced or triggered, then it would represent a novel mechanism
483 not previously recognised for this style of oil extraction at the reported volumes. We have shown

484 that seismic activity can occur at shallow depths in sedimentary basins, especially where pre-
485 existing faults are optimally oriented for reactivation in the regional stress field. This result has
486 implications for understanding the background rate of seismicity close to hydrocarbon
487 exploration targets. Such shallow seismicity could pose a moderate seismic hazard to areas of
488 high population density. Moreover, operators and regulators could consider operating small
489 seismic monitoring networks near conventional oilfield operations to better understand any
490 nearby emergent seismic sequences earlier and to reduce uncertainties.

491 The 2018–19 Newdigate seismic sequence was a contentious issue among members of the public,
492 oilfield operators, and campaign groups. Without detailed seismic observations offered by the
493 installed temporary seismic network and nearby citizen seismology sensors, large uncertainty
494 over the causes of the sequence may have remained for the foreseeable future. Our knowledge
495 of activities at Brockham and HH-1 relies on reported operational data provided by the operators.
496 This source of data remains a controversial issue when determining induced versus natural
497 causes of earthquakes. This particularly applies to industrial activities that lack any precedence
498 for causing earthquakes, and for areas with a low rate of background seismicity. As operations
499 continue in the long term, we recommend seismic monitoring close to hydrocarbon development
500 and production sites, and high-resolution reporting of operational activities (e.g. well shut-in
501 periods), production volumes and rates. Over time, longer-term monitoring could help reduce
502 uncertainties in correlations and causal factors. We have shown that the 2018–2019 Newdigate,
503 Surrey earthquakes offer new insight into the seismogenic potential of shallow sedimentary
504 basins and the seismic hazard associated with these swarms.

505 **Data and resources**

506 All seismic waveform data used in this study is available from the British Geological Survey
507 (<ftp://seiswav.bgs.ac.uk>; last accessed May 2019) and from the RaspberryShake FDSN web
508 service. All instrumentation for the temporary seismic stations was provided by the British
509 Geological Survey. Operational data from Brockham and Horse Hill was provided by the operators
510 of those fields, Angus Energy and UK Oil and Gas, respectively. We made figures using the
511 Matplotlib (Hunter, 2007), GMT (Wessel and Smalley, 1998), and EQcorrscan (Chamberlain *et al.*,
512 2018) packages.

Non-peer reviewed pre-print

513 **Acknowledgments**

514 We thank UK Oil and Gas Plc. and Angus Energy Plc. for providing well data and sonic well logs.
515 We are also grateful to the UK Oil and Gas Authority for organising a workshop on the Newdigate
516 earthquakes, which resulted in very fruitful scientific discussions with all participants. We also
517 thank Branden Christensen and Angel Rodriguez, and their team at RaspberryShake / OSOP, S.A.
518 for their co-operation when working with the community data. We are grateful for discussions
519 with Al Fraser on subsurface fault mapping, and with Antony Butcher on b-value determination.
520 Finally, we thank Mr. Nicholas Booth, the owner of RS station AM.REC60 for continuing to
521 maintain the monitoring effort throughout the Newdigate earthquake sequence. Thank you to
522 David Hawthorn and his team at the BGS for installing the temporary seismic stations.
523 The Authors declare that there are no conflicts of interest.

Non-peer reviewed pre-print

524 **References**

- 525
526 Andrews, I. (2014). The Jurassic shales of the Weald Basin: geology and shale oil and shale gas
527 resource estimation.
528
- 529 Anthony, R. E., A. T. Ringler, D. C. Wilson, and E. Wolin (2018). Do Low-Cost Seismographs
530 Perform Well Enough for Your Network? An Overview of Laboratory Tests and Field
531 Observations of the OSOP Raspberry Shake 4D, *Seismol Res Lett* **90**, no. 1, 219–228, doi:
532 10.1785/0220180251 .
533
- 534 Assumpção, M. (1981). The NW Scotland earthquake swarm of 1974, *Geophys J Int* **67**, no. 3,
535 577–586, doi: 10.1111/j.1365-246x.1981.tb06938.x .
536
- 537 Baptie, B. (2010). Seismogenesis and state of stress in the UK, *Tectonophysics* **482**, no. 1–4, 150
538 159.
539
- 540 Baptie, B., and R. Luckett (2018). The Newdigate earthquake sequence, 2018, British Geological
541 Survey Internal Rept.
542
- 543 Baptie, B., and L. Ottemoeller (2003). The Manchester earthquake swarm of October 2002, *EGS-
544 AGU-EUG Joint Assembly*.
545
- 546 Baptie, B., L. Ottemöller, S. Sargeant, G. Ford, and A. O’Mongain (2005). The Dudley earthquake
547 of 2002: A moderate sized earthquake in the UK, *Tectonophysics* **401**, no. 1–2, 1–22.
548
- 549 Bent, A. L., S. Halchuk, V. Peci, K. E. Butler, K. B. Burke, J. Adams, N. Dahal, and S. Hayek (2017).
550 The McAdam, New Brunswick, Earthquake Swarms of 2012 and 2015–2016: Extremely Shallow,
551 Natural Events, *Seismol Res Lett* **88**, no. 6, 1586–1600, doi: 10.1785/0220170071 .
552
- 553 Bishop, I., P. Styles, and M. Allen (1993). Mining-induced seismicity in the Nottinghamshire
554 Coalfield, *Q J Eng Geol Hydroge* **26**, no. 4, 253–279, doi: 10.1144/gsl.qjegh.1993.026.004.03 .
555
- 556 Butler, M., and C. P. Pullan (1990). Tertiary structures and hydrocarbon entrapment in the
557 Weald Basin of southern England, *Geological Soc Lond Special Publ* **55**, no. 1, 371–391, doi:
558 10.1144/gsl.sp.1990.055.01.19 .
559
- 560 Catalli, F., M. Meier, and S. Wiemer (2013). The role of Coulomb stress changes for injection-
561 induced seismicity: The Basel enhanced geothermal system, *Geophys Res Lett* **40**, no. 1, 72–77,
562 doi: 10.1029/2012gl054147 .
563

- 564 Chamberlain, C. J., C. J. Hopp, C. M. Boese, E. Smith, D. Chambers, S. X. Chu, K. Michailos, and J.
565 Townend (2018). EQcorrscan: Repeating and Near-Repeating Earthquake Detection and
566 Analysis in Python, *Seismol Res Lett* **89**, no. 1, 173 181, doi: 10.1785/0220170151 .
567
- 568 Chang, K., and P. Segall (2016). Seismicity on Basement Faults Induced by Simultaneous Fluid
569 Injection–Extraction, *Pure Appl Geophys* **173**, no. 8, 2621 2636, doi: 10.1007/s00024-016-1319-
570 7 .
571
- 572 Clarke, H., L. Eisner, P. Styles, and P. Turner (2014). Felt seismicity associated with shale gas
573 hydraulic fracturing: The first documented example in Europe, *Geophys Res Lett* **41**, no. 23,
574 8308 8314, doi: 10.1002/2014gl062047 .
575
- 576 Dahm, T., S. Cesca, S. Hainzl, T. Braun, and F. Krüger (2015). Discrimination between induced,
577 triggered, and natural earthquakes close to hydrocarbon reservoirs: A probabilistic approach
578 based on the modeling of depletion-induced stress changes and seismological source
579 parameters, *J Geophys Res Solid Earth* **120**, no. 4, 2491 2509, doi: 10.1002/2014jb011778 .
580
- 581 Davis, S. D., and C. Frohlich (1993). Did (Or Will) Fluid Injection Cause Earthquakes? - Criteria for
582 a Rational Assessment, *Seismological Research Letters* **64**, no. 3–4, 207 224.
583
- 584 Eaton, D. W., N. Igonin, A. Poulin, R. Weir, H. Zhang, S. Pellegrino, and G. Rodriguez (2018).
585 Induced Seismicity Characterization during Hydraulic-Fracture Monitoring with a Shallow-
586 Wellbore Geophone Array and Broadband Sensors, *Seismol Res Lett* **89**, no. 5, 1641 1651, doi:
587 10.1785/0220180055 .
588
- 589 Frohlich, C. (2012). Two-year survey comparing earthquake activity and injection-well locations
590 in the Barnett Shale, Texas, *Proc National Acad Sci* **109**, no. 35, 13934 13938, doi:
591 10.1073/pnas.1207728109 .
592
- 593 Frohlich, C., H. DeShon, B. Stump, C. Hayward, M. Hornbach, and J. I. Walter (2016). A Historical
594 Review of Induced Earthquakes in Texas, *Seismol Res Lett* **87**, no. 4, 1022 1038, doi:
595 10.1785/0220160016 .
596
- 597 Frohlich, C., J. Glidewell, and M. Brunt (2012). Location and Felt Reports for the 25 April 2010
598 mbLg 3.9 Earthquake near Alice, Texas: Was it Induced by Petroleum Production?The April 2010
599 Earthquake near Alice, Texas: Was it Induced by Petroleum Production?, *B Seismol Soc Am* **102**,
600 no. 2, 457 466, doi: 10.1785/0120110179 .
601
- 602 García-Moreno, D., K. Verbeeck, T. Camelbeeck, Batist, F. Oggioni, Z. O. Hurtado, W. Versteeg,
603 H. Jomard, J. Collier, S. Gupta, *et al.* (2015). Fault activity in the epicentral area of the 1580
604 Dover Strait (Pas-de-Calais) earthquake (northwestern Europe), *Geophys J Int* **201**, no. 2, 528–
605 542, doi: 10.1093/gji/ggv041 .

- 606
607 Goebel, T. H., and E. E. Brodsky (2018). The spatial footprint of injection wells in a global
608 compilation of induced earthquake sequences, *Science* **361**, no. 6405, 899 904, doi:
609 10.1126/science.aat5449 .
610
611 González, P. J., K. F. Tiampo, M. Palano, F. Cannavó, and J. Fernández (2012). The 2011 Lorca
612 earthquake slip distribution controlled by groundwater crustal unloading, *Nat Geosci* **5**, no. 11,
613 821 825, doi: 10.1038/ngeo1610 .
614
615 Grigoli, F., S. Cesca, E. Priolo, A. Rinaldi, J. F. Clinton, T. A. Stabile, B. Dost, M. Fernandez, S.
616 Wiemer, and T. Dahm (2017). Current challenges in monitoring, discrimination, and
617 management of induced seismicity related to underground industrial activities: A European
618 perspective, *Reviews of Geophysics* **55**, no. 2, 310 340.
619
620 Grünthal, G. (1998). European macroseismic scale 1998.
621
622 Hansen, D. L., D. J. Blundell, and S. B. Nielsen (2002). A model for the evolution of the Weald
623 Basin, *Bulletin of the Geological Society of Denmark*.
624
625 Häring, M. O., U. Schanz, F. Ladner, and B. C. Dyer (2008). Characterisation of the Basel 1
626 enhanced geothermal system, *Geothermics* **37**, no. 5, 469 495, doi:
627 10.1016/j.geothermics.2008.06.002 .
628
629 Heimann, S. (2016). Sebastian Heimann / lassie.
630
631 Horton, S. (2012). Disposal of Hydrofracking Waste Fluid by Injection into Subsurface Aquifers
632 Triggers Earthquake Swarm in Central Arkansas with Potential for Damaging Earthquake,
633 *Seismol Res Lett* **83**, no. 2, 250 260, doi: 10.1785/gssrl.83.2.250 .
634
635 Hough, S. (2014). Shaking from Injection-Induced Earthquakes in the Central and Eastern United
636 States, *B Seismol Soc Am* **104**, no. 5, 2619 2626, doi: 10.1785/0120140099 .
637
638 Hunter, J. D. (2007). Matplotlib: A 2D graphics environment, *Computing in science &*
639 *engineering* **9**, no. 3, 90.
640
641 Kaven, J., S. Hickman, A. McGarr, and W. Ellsworth (2015). Surface Monitoring of
642 Microseismicity at the Decatur, Illinois, CO 2 Sequestration Demonstration Site, *Seismol Res Lett*
643 **86**, no. 4, 1096 1101, doi: 10.1785/0220150062 .
644
645 Keranen, K., M. Weingarten, G. Abers, Bekins, and S. Ge (2014). Sharp increase in central
646 Oklahoma seismicity since 2008 induced by massive wastewater injection, *Science* **345**, no.
647 6195, 448 451, doi: 10.1126/science.1255802 .

- 648
649 Kuszniir, N., D. Ashwin, and A. Bradley (1980). Mining induced seismicity in the North
650 Staffordshire coalfield, England, *International Journal of Rock Mechanics and Mining Sciences &*
651 *Geomechanics Abstracts* **17**, no. 1, 45 55.
652
- 653 Lomax, A., A. Michelini, and A. Curtis (2009). Earthquake location, Direct, Global-search
654 Methods, *Encyclopedia of complexity and systems science*, 2449 2473, doi: 10.1007/978-0-387-
655 30440-3_150 .
656
- 657 Luckett, R., L. Ottemöller, A. Butcher, and B. Baptie (2019). Extending local magnitude ML to
658 short distances, *Geophys J Int* **216**, no. 2, 1145 1156, doi: 10.1093/gji/ggy484 .
659
- 660 Maceira, M., C. J. Ammon, and R. Herrmann (2000). Faulting Parameters of the September 25,
661 1998 Pymatuning, Pennsylvania Earthquake, *Seismol Res Lett* **71**, no. 6, 742 752, doi:
662 10.1785/gssrl.71.6.742 .
663
- 664 Malone, S., G. Rothe, and S. W. Smith (1975). Details of microearthquake swarms in the
665 Columbia Basin, Washington, *Am J Sci* **259**, no. 8, doi: 10.2475/ajs.259.8.583 .
666
- 667 Maury, V., J. Grasso, and G. Wittlinger (1990). Lacq Gas Field (France): Monitoring of Induced
668 Subsidence and Seismicity Consequences on Gas Production and Field Operation, doi:
669 10.2118/20887-ms .
670
- 671 Maxwell, S., M. Jones, R. Parker, S. Miong, S. Leaney, D. Dorval, D. D'Amico, J. Logel, E.
672 Anderson, and K. Hammermaster (2012). Fault activation during hydraulic fracturing, *SEG*
673 *Technical Program Expanded Abstracts 2009* **43**, 1552 1556, doi: 10.1190/1.3255145 .
674
- 675 McNamara, D., H. Benz, R. Herrmann, E. Bergman, P. Earle, A. Holland, R. Baldwin, and A.
676 Gassner (2015). Earthquake hypocenters and focal mechanisms in central Oklahoma reveal a
677 complex system of reactivated subsurface strike-slip faulting, *Geophys Res Lett* **42**, no. 8, 2742–
678 2749, doi: 10.1002/2014gl062730 .
679
- 680 Musson, R. (1994). A catalogue of British earthquakes, *British Geological Survey Global*
681 *Seismology Report*.
682
- 683 Musson, R. M. W. (1993). Comrie: a historical scottish earthquake swarm and its place in the
684 history of seismology, *Terra Nova* **5**, no. 5, 477–480, doi: 10.1111/j.1365-3121.1993.tb00288.x .
685
- 686 Musson, R. (2008). The seismicity of the British Isles to 1600, *British Geological Survey Open*
687 *Report*.
688
- 689 Musson, R., and S. Sargeant (2007). Eurocode 8 seismic hazard zoning maps for the UK.

- 690
691 Ottemöller, L., B. Baptie, and N. Smith (2009). Source Parameters for the 28 April 2007 Mw 4.0
692 Earthquake in Folkestone, United Kingdom, *B Seismol Soc Am* **99**, no. 3, 1853–1867, doi:
693 10.1785/0120080244 .
694
695 Ottemöller, L., H. Nielsen, K. Atakan, J. Braunmiller, and J. Havskov (2005). The 7 May 2001
696 induced seismic event in the Ekofisk oil field, North Sea, *J Geophys Res Solid Earth* **110**,
697 no. B10, 379, doi: 10.1029/2004jb003374 .
698
699 Ottemöller, L., and C. Thomas (2007). Highland Boundary Fault Zone: Tectonic implications of
700 the Aberfoyle earthquake sequence of 2003, *Tectonophysics* **430**, no. 1–4, 83–95.
701
702 Pine, R., and A. Batchelor (2001). Downward migration of shearing in jointed rock during
703 hydraulic injections, *International Journal of Rock Mechanics and Mining Sciences &*
704 *Geomechanics Abstracts* **21**, no. 5, 249–263.
705
706 Redmayne, D. (1988). Mining induced seismicity in UK coalfields identified on the BGS National
707 Seismograph Network, *Geological Soc Lond Eng Geology Special Publ* **5**, no. 1, 405–413, doi:
708 10.1144/gsl.eng.1988.005.01.45 .
709
710 Rubinstein, J. L., and A. Mahani (2015). Myths and Facts on Wastewater Injection, Hydraulic
711 Fracturing, Enhanced Oil Recovery, and Induced Seismicity, *Seismol Res Lett* **86**, no. 4,
712 1060–1067, doi: 10.1785/0220150067 .
713
714 Schultz, R., R. Wang, Y. Gu, H. K. of Geophysical, and 2017 (2016). A seismological overview of
715 the induced earthquakes in the Duvernay play near Fox Creek, Alberta, *Wiley Online Library*.
716
717 Segall, P. (1989). Earthquakes triggered by fluid extraction, *Geology* **17**, no. 10, 942, doi:
718 10.1130/0091-7613(1989)017<0942:etbfe>2.3.co;2 .
719
720 Segall, P., and S. D. Fitzgerald (1998). A note on induced stress changes in hydrocarbon and
721 geothermal reservoirs, *Tectonophysics* **289**, no. 1–3, 117–128, doi: 10.1016/s0040-
722 1951(97)00311-9 .
723
724 Sileny, J. (2009). Resolution of Non-Double-Couple Mechanisms: Simulation of Hypocenter
725 Mislocation and Velocity Structure Mismodeling, *B Seismol Soc Am* **99**, no. 4, 2265–2272, doi:
726 10.1785/0120080335 .
727
728 Staudenmaier, N., T. Tormann, B. Edwards, N. Deichmann, and S. Wiemer (2018). Bilinearity in
729 the Gutenberg-Richter Relation Based on ML for Magnitudes Above and Below 2, From
730 Systematic Magnitude Assessments in Parkfield (California), *Geophys Res Lett* **45**, no. 14,
731 6887–6897, doi: 10.1029/2018gl078316 .

- 732
733 Steacy, S., D. Marsan, S. S. Nalbant, and J. McCloskey (2004). Sensitivity of static stress
734 calculations to the earthquake slip distribution, *J Geophys Res Solid Earth* 1978 2012 **109**, no.
735 B4, 20,153, doi: 10.1029/2002jb002365 .
736
737 Survey, B. (2010). Detection Capability,
738 <http://www.earthquakes.bgs.ac.uk/monitoring/detection-capability.html>.
739
740 Teufel, L. W., D. W. Rhett, and H. E. Farrell (1991). Effect of reservoir depletion and pore
741 pressure drawdown on in situ stress and deformation in the Ekofisk field, North Sea, *The 32nd*
742 *US Symposium on Rock Mechanics (USRMS)*.
743
744 UKOGL (2019). UK Onshore Geophysical Library.
745
746 Verdon, J. P. (2014). Significance for secure CO₂ storage of earthquakes induced by fluid
747 injection, *Environ Res Lett* **9**, no. 6, 064022, doi: 10.1088/1748-9326/9/6/064022 .
748
749 Verdon, J. P., B. J. Baptie, and J. J. Bommer (2019). An Improved Framework for Discriminating
750 Seismicity Induced by Industrial Activities from Natural Earthquakes, *Seismol Res Lett*, doi:
751 10.1785/0220190030 .
752
753 Verdon, J. P., J.-M. Kendall, A. Butcher, R. Luckett, and B. J. Baptie (2018). Seismicity induced by
754 longwall coal mining at the Thoresby Colliery, Nottinghamshire, U.K., *Geophys J Int* **212**, no. 2,
755 942 954, doi: 10.1093/gji/ggx465 .
756
757 Waldhauser, F., and W. L. Ellsworth (2000). A Double-Difference Earthquake Location
758 Algorithm: Method and Application to the Northern Hayward Fault, California, *B Seismol Soc*
759 *Am* **90**, no. 6, 1353 1368, doi: 10.1785/0120000006 .
760
761 Wang, R., Y. Gu, R. Schultz, and Y. Chen (2018). Faults and Non-Double-Couple Components for
762 Induced Earthquakes, *Geophys Res Lett* **45**, no. 17, 8966 8975, doi: 10.1029/2018gl079027 .
763
764 Wees, V. J., L. Buijze, K. van Thienen-Visser, M. Nepveu, B. Wassing, B. Orlic, and P. Fokker
765 (2014). Geomechanics response and induced seismicity during gas field depletion in the
766 Netherlands, *Geothermics* **52**, 206 219, doi: 10.1016/j.geothermics.2014.05.004 .
767
768 Wessel, P., and R. Smalley (1998). New, improved version of generic mapping tools released,
769 *Eos Trans. AGU* **79**, no. 47, 579 579.
770
771 Wiemer, S., and M. Wyss (2000). Minimum Magnitude of Completeness in Earthquake Catalogs:
772 Examples from Alaska, the Western United States, and Japan, *B Seismol Soc Am* **90**, no. 4, 859–
773 869, doi: 10.1785/0119990114 .

- 774
775 Willacy, C., E. van Dedem, S. Minisini, J. Li, J. Blokland, I. Das, and A. Droujinine (2018).
776 Application of full-waveform event location and moment-tensor inversion for Groningen
777 induced seismicity, *Lead Edge* **37**, no. 2, 92 99, doi: 10.1190/tle37020092.1 .
778
- 779 Wilson, M. P., R. J. Davies, G. R. Foulger, B. R. Julian, P. Styles, J. G. Gluyas, and S. Almond
780 (2015). Anthropogenic earthquakes in the UK: A national baseline prior to shale exploitation,
781 *Mar Petrol Geol* **68**, no. Bull. Earthq. Res. Inst. Tokyo Univ. 43 1965, 1 17, doi:
782 10.1016/j.marpetgeo.2015.08.023 .
783
- 784 Wyss, M., K. Shimazaki, and S. Wiemer (1997). Mapping active magma chambers by b values
785 beneath the off-Ito volcano, Japan, *J Geophys Res Solid Earth* **102**, no. B9, 20413 20422, doi:
786 10.1029/97jb01074 .
787
- 788 Zbinden, D., A. Rinaldi, L. Urpi, and S. Wiemer (2017). On the physics-based processes behind
789 production-induced seismicity in natural gas fields, *J Geophys Res Solid Earth* **122**, no. 5, 3792
790 3812, doi: 10.1002/2017jb014003 .
791
- 792 Zhang, H., D. W. Eaton, G. Li, Y. Liu, and R. M. Harrington (2016). Discriminating induced
793 seismicity from natural earthquakes using moment tensors and source spectra, *J Geophys Res*
794 *Solid Earth* **121**, no. 2, 972 993, doi: 10.1002/2015jb012603 .

795 **Figure captions**

796 Figure 1: Regional context showing the study area (brown rectangle), together with instrumental
797 and historical seismicity context of England and Wales from the BGS catalogue. Induced
798 earthquakes are from Wilson et al. (Wilson *et al.*, 2015) Regional seismic stations used in this
799 study are shown. Mapped surface fault traces come from BGS
800 (https://www.bgs.ac.uk/data/services/kml/BGS_GEOLOGY_625_faults.kmz; last accessed May
801 2019). Past earthquake focal mechanisms (orange beachballs) come from Baptie, 2010 and from
802 BGS annual earthquake bulletin reports. Labels a) and b) refer to the 2005 Billingshurst and 1811–
803 1834 Chichester sequence, respectively, which are discussed in the text.

804 Figure 2: Left: map of the study area showing relocated earthquakes of the 2018–2019 Newdigate
805 sequence, focal mechanisms, mapped faults, local seismic stations, 2-D seismic lines (Note S6 in
806 the electronic supplement to this article), and the locations of oilfield activities. Only high-quality
807 earthquake hypocentres are plotted with a maximum azimuthal gap of less than 200°.
808 Earthquake locations are coloured to show their evolution through time. Dark grey circles
809 indicate earthquakes that occurred before the installation of the temporary local seismic
810 network, and therefore have uncertain locations, with fixed depths. 2-D seismic profile TWLD-
811 90-15 is shown in Figure 6. Right: N-S and W-E cross-sections of seismicity with event
812 hypocentres. The cross-section locations are labelled on the map. The definition of fault
813 abbreviations are as follows: BHF = Box Hill Fault; BRF = Brockham Fault; BUF = Buckland Fault;
814 COF = Collendean Fault; FGF = Faygate Fault; HWF = Holmwood Fault; HHF = Horse Hill Fault; KFF

815 = Kingsfold Fault; LHF = Leigh Fault; NGF = Newdigate Fault; OKF = Ockley Fault; WCF = Westcott
816 Fault; WB1F = Whiteberry-1 Fault.

817 Figure 3: Timeline comparing evolution of the Newdigate seismic swarm with nearby oil field
818 activities. a) Installation dates of the local temporary seismic monitoring network. (a) detected
819 seismicity, cumulative number of events, and the grey shaded area indicating the approximate
820 completeness magnitude of the catalogue over time. (c) Horse Hill-1: operations timeline (shaded
821 boxes) together with flow-period averaged production and cumulative production over time. d)
822 Daily reservoir production and injection values at Brockham. (e) A long-term view of operations,
823 with the time interval shown in panels above covering the 2018–2019 period delineated by the
824 grey box and connecting lines.

825 Figure 4: Lowpass-filtered (10 Hz) vertical-component waveforms recorded at RaspberryShake
826 (RS) station REC60 (~8 km epicentral distance) showing similarity between the largest events (M_L
827 > 1.5) of the Newdigate sequence. Waveform cross-correlation (CC) values computed in a
828 window starting 0.02 s and ending 0.70 s after the picked P-wave arrival are labelled and are
829 calculated with respect to the first event in the sequence (#1).

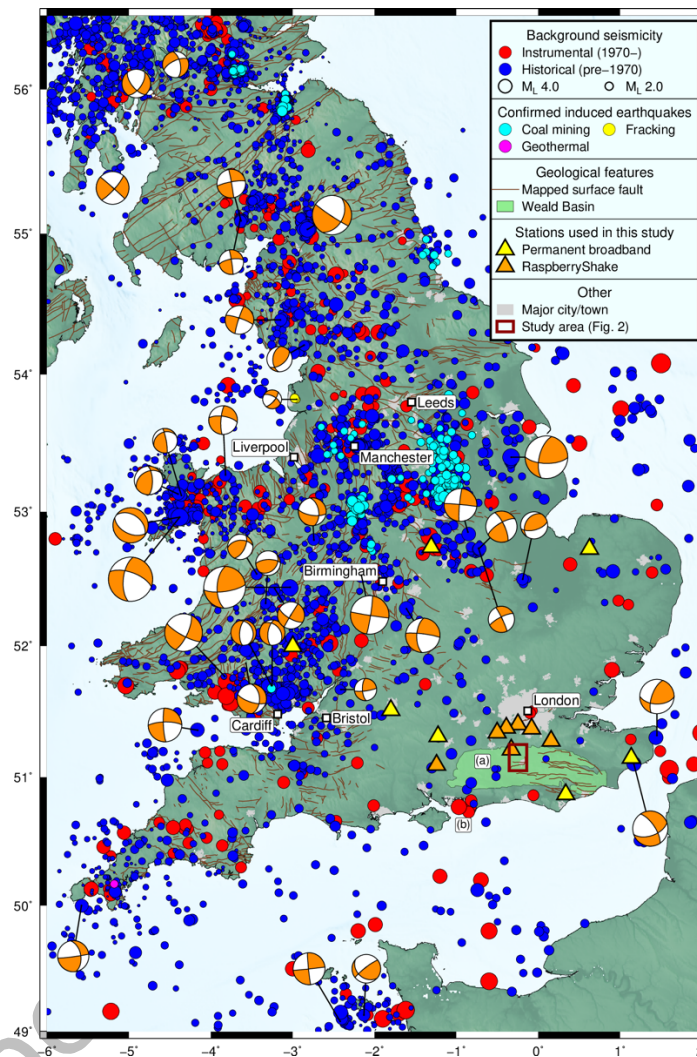
830 Figure 5: a) and b) Moment tensor solutions for two earthquakes observed by local stations. i)
831 Map showing stations and best-fitting focal mechanism; ii) waveform correlation as a function of
832 centroid depth; iii) waveform fits. “VR” = variance reduction. c) Observed first-motion P-wave
833 polarities compared to faults planes from the best-fitting focal mechanisms from moment
834 tensors a) and b).

835 Figure 6: 2-D seismic section along profile TWLD-90-15 (Figure 2) showing interpreted faults
836 (green lines), geological formations, together with the projected positions of relocated
837 earthquakes from this study. Poorly constrained event with fixed depths are shown as squares;
838 well-constrained events are shown as circles. Event location are also given as dashed error bars.
839 COF = C = Collendean Fault; FGF = Faygate Fault; LHF = Leigh Fault; NGF = Newdigate Fault.

840 Figure 7: Individual and cumulative frequency-magnitude distributions together with Gutenberg-
841 Richter (G-R) relationship fits for a) the entire sequence and b) the sequence recorded by the
842 temporary local monitoring network, with magnitudes scaled to an equivalent M_w , and G-R fits
843 truncated to maximum magnitude of 1.2.

Non-peer reviewed pre-print

844 **Figures**



845

846 Figure 1: Regional context showing the study area (brown rectangle), together with instrumental and
847 historical seismicity context of England and Wales from the BGS catalogue. Induced earthquakes are
848 from Wilson et al. (Wilson *et al.*, 2015) Regional seismic stations used in this study are shown. Mapped
849 surface fault traces come from BGS
850 (https://www.bgs.ac.uk/data/services/kml/BGS_GEOLOGY_625_faults.kmz; last accessed May 2019).
851 Past earthquake focal mechanisms (orange beachballs) come from Baptie, 2010 and from BGS annual
852 earthquake bulletin reports. Labels a) and b) refer to the 2005 Billingshurst and 1811–1834 Chichester
853 sequence, respectively, which are discussed in the text.

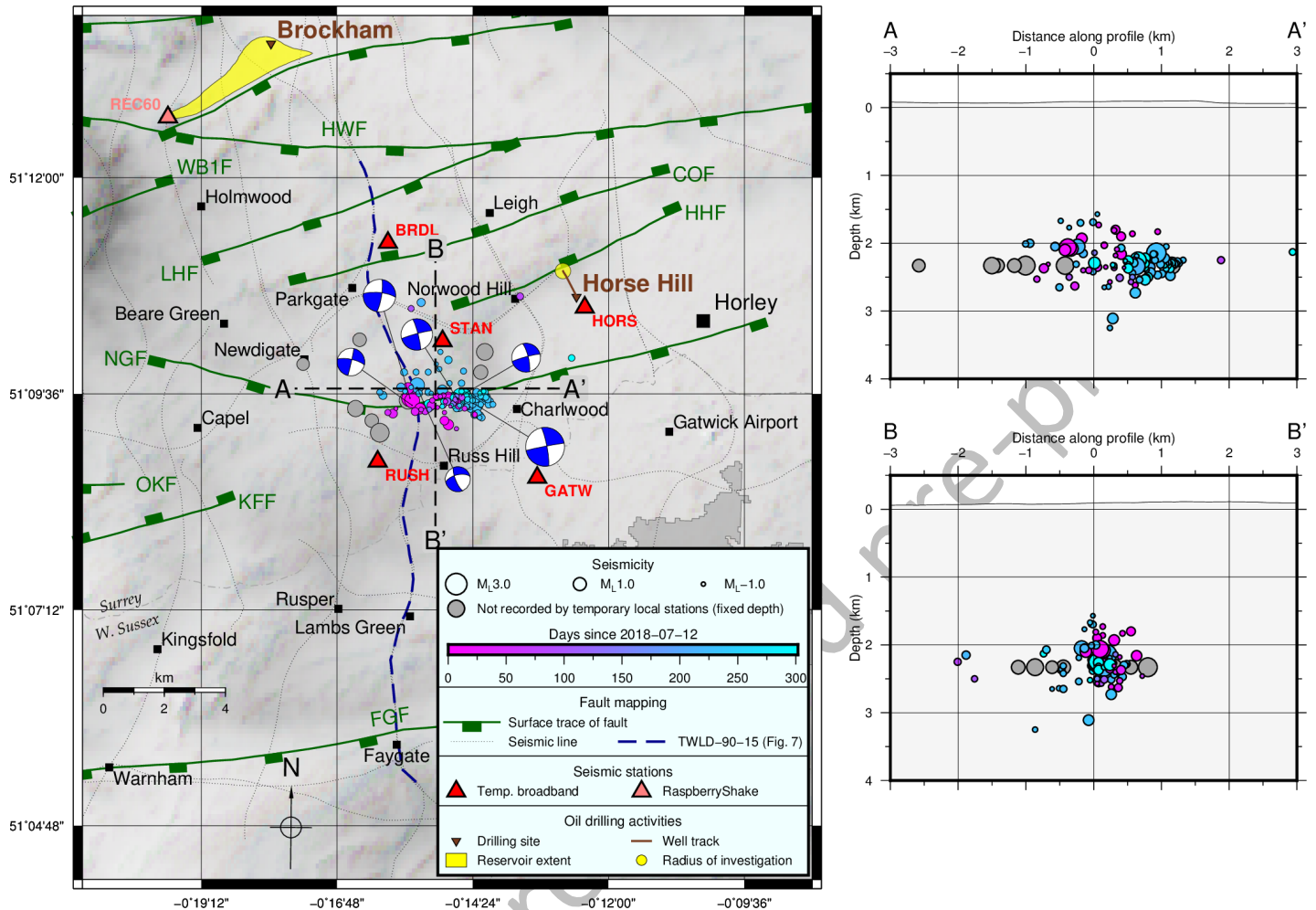


Figure 2: Left: map of the study area showing relocated earthquakes of the 2018–2019 Newdigate sequence, focal mechanisms, mapped faults, local seismic stations, 2-D seismic lines (Note S6 in the electronic supplement to this article), and the locations of oilfield activities. Only high-quality earthquake hypocentres are plotted with a maximum azimuthal gap of less than 200°. Earthquake locations are coloured to show their evolution through time. Dark grey circles indicate earthquakes that occurred before the installation of the temporary local seismic network, and therefore have uncertain locations, with fixed depths. 2-D seismic profile TWLD-90-15 is shown in Figure 6. Right: N-S and W-E cross-sections of seismicity with event hypocentres. The cross-section locations are labelled on the map. The definition of fault abbreviations are as follows: BHF = Box Hill Fault; BRF = Brockham Fault; BUF = Buckland Fault; COF = Collendean Fault; FGF = Faygate Fault; HWF = Holmwood Fault; HHF = Horse Hill Fault; KFF = Kingsfold Fault; LHF = Leigh Fault; NGF = Newdigate Fault; OKF = Ockley Fault; WCF = Westcott Fault; WB1F = Whiteberry-1 Fault.

a) Local seismic network installation

Findings are subject to change.

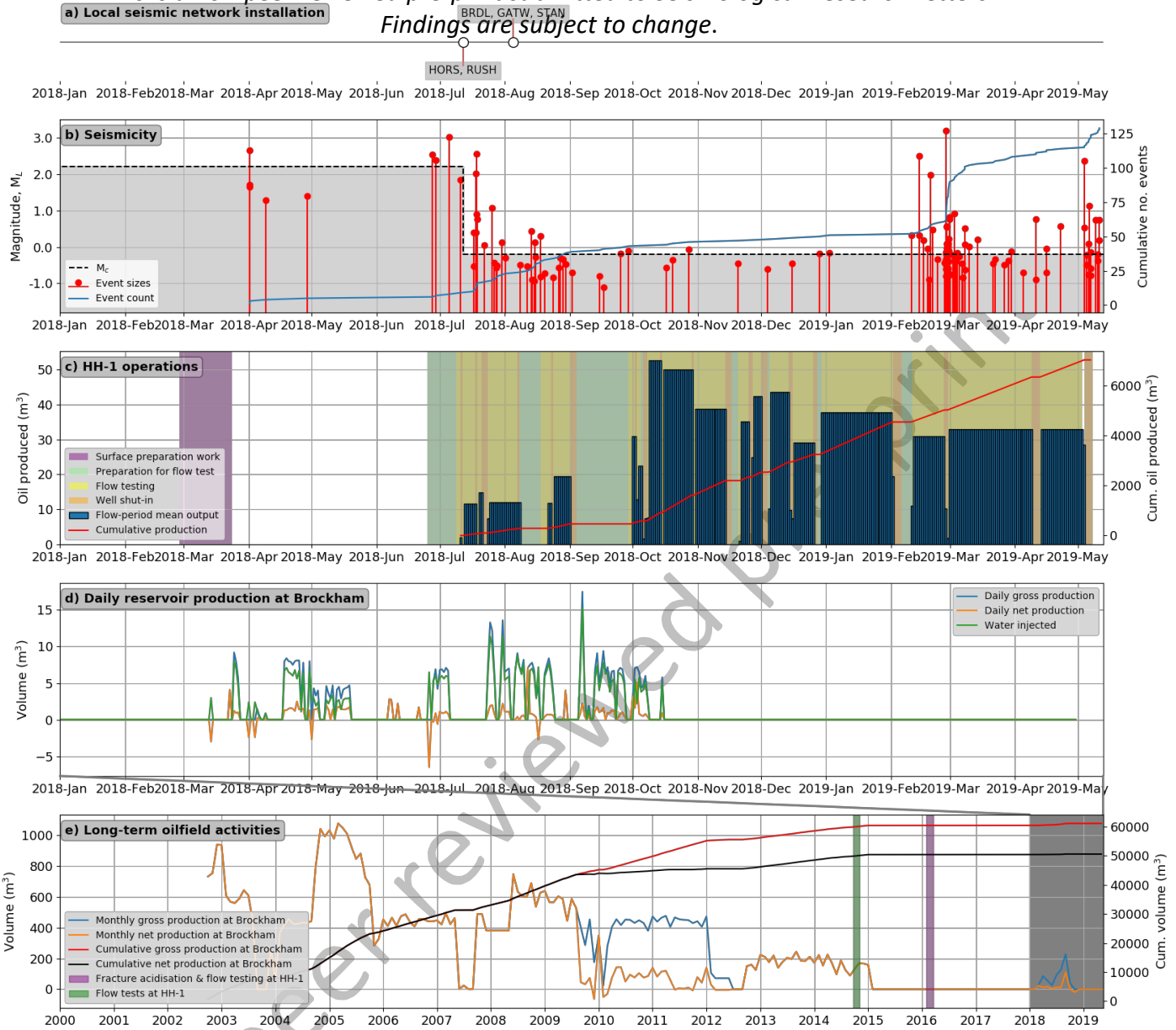
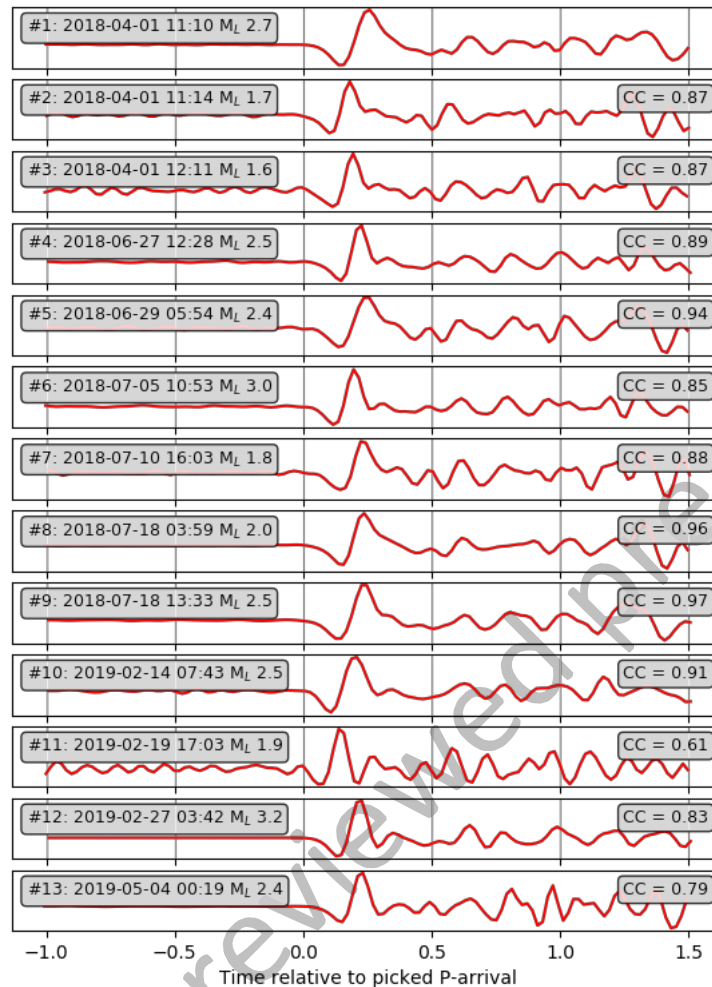


Figure 3: Timeline comparing evolution of the Newdigate seismic swarm with nearby oil field activities. a) Installation dates of the local temporary seismic monitoring network. (a) detected seismicity, cumulative number of events, and the grey shaded area indicating the approximate completeness magnitude of the catalogue over time. (c) Horse Hill-1: operations timeline (shaded boxes) together with flow-period averaged production and cumulative production over time. (d) Daily reservoir production and injection values at Brockham. (e) A long-term view of operations, with the time interval shown in panels above covering the 2018–2019 period delineated by the grey box and connecting lines.



856

857 Figure 4: Lowpass-filtered (10 Hz) vertical-component waveforms recorded at RaspberryShake (RS)
858 station REC60 (~8 km epicentral distance) showing similarity between the largest events ($M_L > 1.5$) of
859 the Newdigate sequence. Waveform cross-correlation (CC) values computed in a window starting 0.02 s
860 and ending 0.70 s after the picked P-wave arrival are labelled and are calculated with respect to the first
861 event in the sequence (#1).

a) 2019-02-14 07:43:32.84 Mw 2.5

Filter: 0.4 - 0.8 Hz
Findings are subject to change.

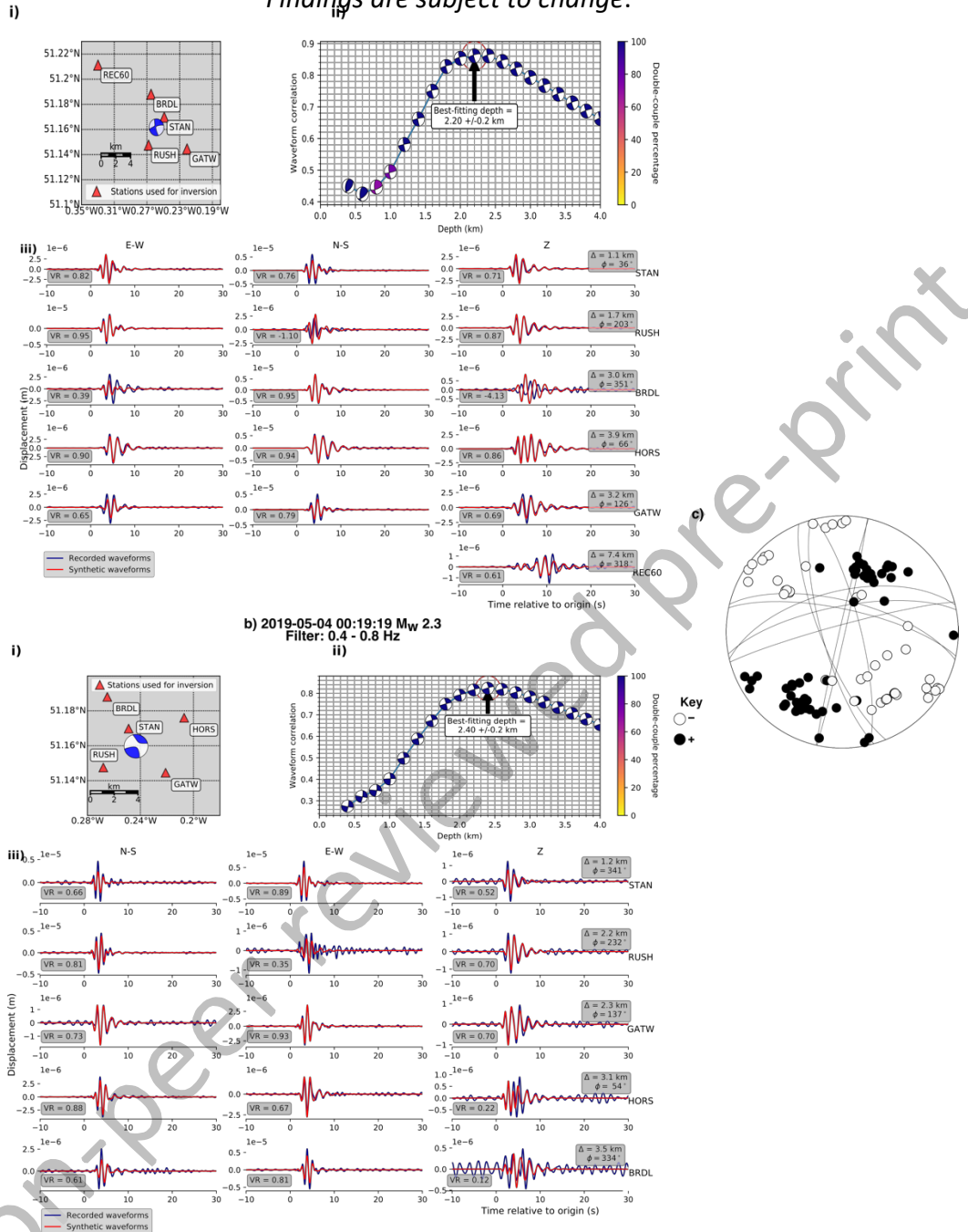


Figure 5: a) and b) Moment tensor solutions for two earthquakes observed by local stations. i) Map showing stations and best-fitting focal mechanism; ii) waveform correlation as a function of centroid depth; iii) waveform fits. “VR” = variance reduction. c) Observed first-motion P-wave polarities compared to faults planes from the best-fitting focal mechanisms from moment tensors a) and b).

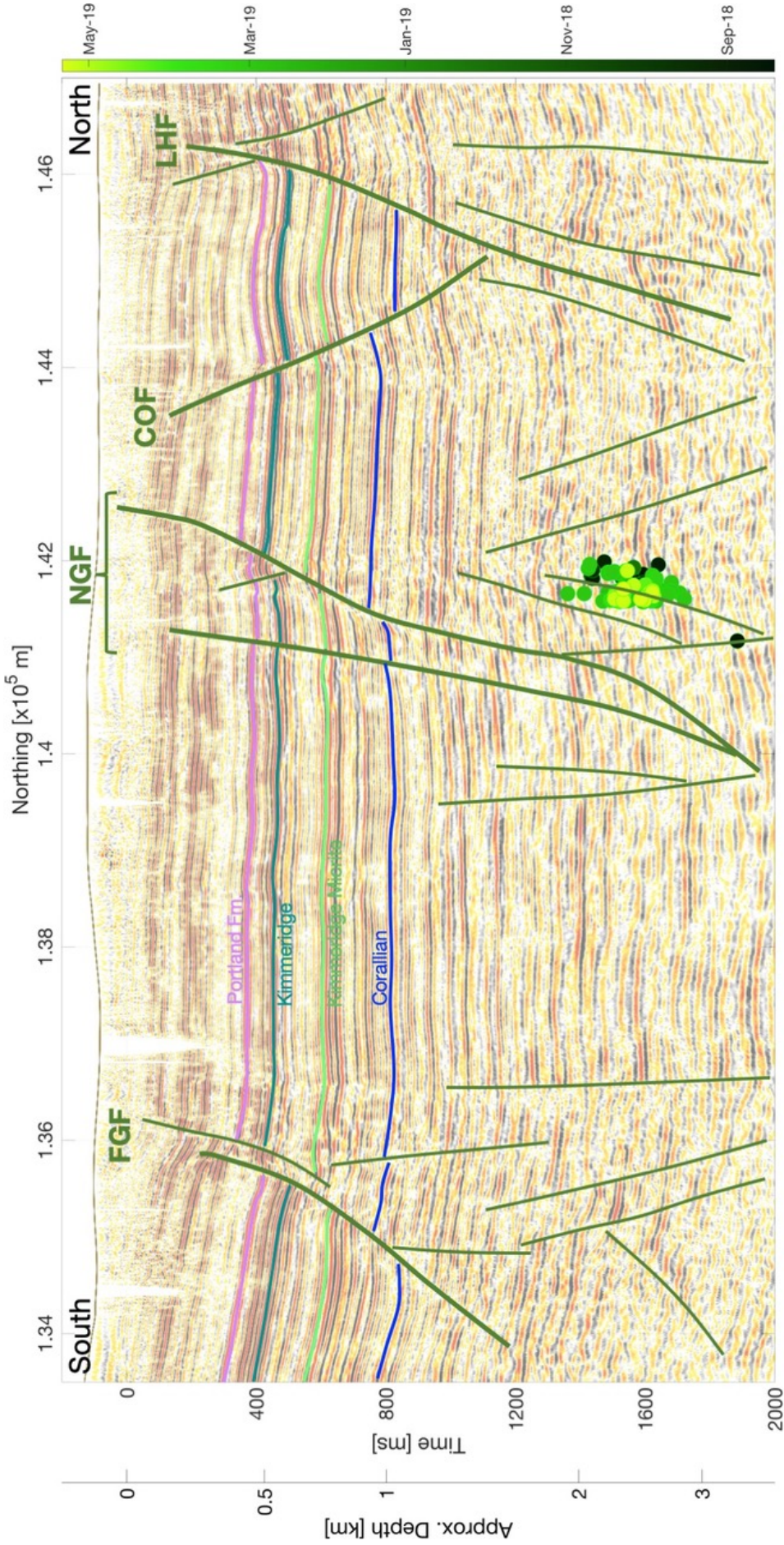


Figure 6: 2-D seismic section along profile TWLD-90-15 (Figure 2) showing interpreted faults (green lines), geological formations, together with the projected positions of relocated earthquakes from this study. Poorly constrained event with fixed depths are shown as squares; well-constrained events are shown as circles. Event location are also given as dashed error bars. COF = C = Collendean Fault; FGF = Faygate Fault; LHF = Leigh Fault; NGF = Newdigate Fault.

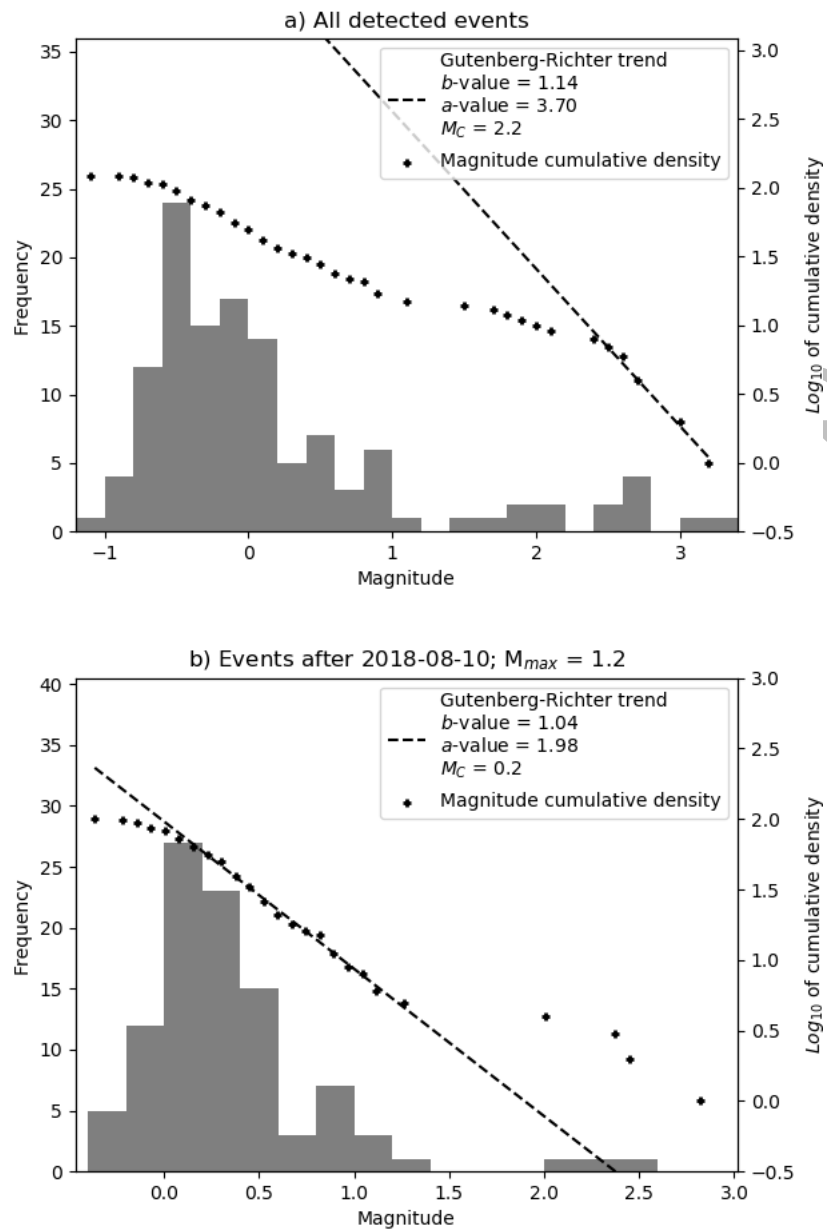


Figure 7: Individual and cumulative frequency-magnitude distributions together with Gutenberg-Richter (G-R) relationship fits for a) the entire sequence and b) the sequence recorded by the temporary local monitoring network, with magnitudes scaled to an equivalent M_w , and G-R fits truncated to maximum magnitude of 1.2.

Supplementary Notes

S1 Velocity model and relocation

We need a robust velocity model for well-constrained earthquake locations, and to make sure no systematic errors bias the hypocentral locations. A 1-D seismic velocity model should represent the average structure along each seismic ray-path, especially close to the source. We based our initial 1-D velocity model on constraints from the BGS's "General UK" operational model and the CRUST1.0 model (Laske *et al.*, 2013) for south-east England. We then improved this using sonic logs from the Brockham (UKOGL, 2019) and Horse Hill wells (UKOG, personal communication). We tried different layer thicknesses and seismic velocity perturbations in terms of the stability of event locations, spatial clustering of events, and the average residual between observed and theoretical seismic wave arrival times. We also experimented with including a depth-varying S-wave velocity model based on Poisson's ratio constraints at the nearby Balcombe Well (UKOG, personal communication). Overall, we found that a depth-varying shear-wave velocity resulted in higher arrival time residuals, so we used a constant v_p/v_s ratio of 1.73, as per the BGS operational model, which is consistent with Wadati plot analysis. Figure S1 and Table S1 in the electronic supplement to this article show our preferred 1-D layered velocity model.

We re-picked P- and S-wave arrival times from all events, classifying the error on each pick because of arrival time uncertainty from 0 to 4 (where 0 shows the smallest error of ~ 0.1 s and 4 is the largest error of > 1.5 s). We performed iterative picking and initial relocation of events using the SDX software package (Hicks *et al.*, 2014).

For the events recorded by only two temporary stations, we found that inclusion of stations at longer epicentral distances (> 25 km) resulted in poorly constrained depths, even though we applied a distance weighting to observations in the relocation strategy (Theunissen *et al.*, 2018).

Even with an appropriate velocity model, local RS stations, and our relocation strategy, events that occurred before the installation of the dedicated local network had poorly constrained hypocentre parameters, with depths ranging from 0 km to 2.4 km and mean depth uncertainties of ± 1.5 km. Because of this inherent uncertainty for the earlier events in the sequence, we first focussed on the events recorded by all five local temporary stations had recorded.

For double-difference relocation, we used a combination of phase arrival times and waveform cross-correlations for both P- and S-waves. We used the software toolbox, hypoDDpy (Krischer, 2015). Waveform cross-correlation values were computed on windows of data starting 0.05 s before the picked arrival time and ending 0.20 s after the picked arrival time. Data windows were bandpass filtered between 1.5 and 20.0 Hz. The relocated origins were inverted for using singular value decomposition.

Station GATW suffered from timing problems from the period 12/23/2018 to 27/03/2019. Therefore, we used S-P relative observations for the single-event locations for earthquakes within this period. For the double-difference relocation, we excluded absolute arrival times and cross-correlation data from this station during the above time period.

S2 Magnitude estimation

We computed event magnitudes from the largest zero-to-peak displacement in nanometres on 3-component waveforms in a window starting at the P-wave arrival and ending at a time of 30 seconds after the theoretical Lg arrival time (assuming a minimum Lg velocity of 3 km/s). Waveforms were high-pass filtered at 1.25 Hz, and we only used waveforms with a signal-to-noise ratio of greater than 2. We used the largest amplitude of all station components (this allowed the use of measurements from single-component RS stations) to calculate station magnitudes using the scale of Lockett et al. (2019), which builds on Butcher et al. (2017) to account for near-field amplitude attenuation and the scale of Ottemöller and Sergeant (2013) for regional distances. We then computed the overall event magnitude using a 25% trimmed mean to reject outliers. This magnitude scale is largely based on existing data, and as a result, significant residuals may be expected in areas with few earthquakes and recording stations such as south-east England.

S3 Waveform moment tensor inversion

For long-period waveform inversion, we use the ISOLA software (Sokos and Zahradnik, 2007), which uses a least-squares inversion to solve for moment tensor point-sources, with a grid search to solve for the best-fitting centroid time and position of trial point-sources. We fix the centroid location at the hypocentre position and allow centroid depth to vary with an interval of 200 m. We computed Greens Functions using the frequency-wavenumber algorithm of Bouchon (1981) using the layered velocity model described above (Figure S1). Because of the relatively small

magnitude of the events, and proximity of the local stations (<8 km epicentral distance), we filtered the waveforms at relatively high frequencies (0.33 – 1.0 Hz). We cross-checked the best-fitting moment tensor solutions with observed first-motion polarities. We also checked stability and uncertainty of moment tensor solutions by jack-knifing waveform data. We found that the resulting moment magnitudes are in excellent agreement with the computed local magnitudes. A similar good correlation is found between centroid and hypocentre depths (Figure S7b) in the electronic supplement to this article).

S4 Stress drop estimates from displacement spectra

We computed stress drops for the largest events of the sequence ($M_L \geq 2.0$) by fitting source amplitude spectra using a Brune source model following the approach of Ottemöller & Havskov (2016), which has been successfully applied to UK earthquakes (Ottemöller *et al.*, 2009). We used records at short epicentral distance (< 8 km) from microseismic events ($M_L < 1.5$) to determine site attenuation, κ using the displacement-slope method (Kilb *et al.*, 2012) at frequencies of 2.5-15 Hz - well below the expected corner frequency for these event magnitudes. We found a mean κ of 0.02, consistent with the results of Ottemöller *et al.* (2009) for the 2007 Folkestone earthquake, with stations located in south-eastern England. We used an UK-average attenuation model documented in Ottemöller *et al.* (2009). To negate the effect of weaker signal quality and greater regional attenuation effects at longer distances, we only computed corner frequencies and moment magnitudes at local seismic stations (< 8 km distance).

S5 Static (Coulomb stress modelling)

Using the earthquake locations, focal mechanisms and the mapping of faults from seismic profiles, static (Coulomb) stress changes from the largest earthquakes ($M > 2$) in the sequence were calculated. The static stress is defined by Equation 1:

$$\Delta CST = \Delta\tau - \mu(\Delta\sigma + \Delta P) \quad (\text{Eq.1})$$

where ΔCST is the Coulomb stress transfer, $\Delta\tau$ is the change in shear stress (in the direction of fault slip), μ is the coefficient of friction, $\Delta\sigma$ is the change in normal stress and ΔP is the change in pore fluid pressure (Harris and Simpson, 1992, 1998). Herein we do not consider changes in pore fluid pressure when calculating the static stress change because we lack direct measurements of this at the depths the earthquakes occurred at. In addition, if the sequence can be explained by static stress triggering alone without invoking pore fluid pressure changes, then this would suggest a natural cause to these earthquakes. Poro-elastic stress changes have been suggested to trigger earthquakes by injection (Segall and Lu, 2015). These calculations were performed using Coulomb 3.4 (Toda *et al.*, 2005). Uniform slip on square faults were modelled because of the lack of information of detailed slip distribution of fault plane size/geometry. This will affect our interpretation when earthquake epicentres are located close together (Steady *et al.*, 2004).

There are a number of uncertainties in these models, primarily regarding the fault geometry/orientation. To account for this, the static stresses have been resolved onto fault geometries consistent with the Newdigate and Horse Hill faults, and optimally orientated strike-

slip and thrust faults (given a regional stress tensor from Baptie (2010) with sigma-1 orientated NW-SE).

S6 Fault mapping from 2-D seismic profiles

A selection of 2-D seismic lines was provided by the UK Onshore Geophysical Library (Figure 2) and acquired in this area since the early 1960s. We only used surveys acquired from the late 1970s onwards in our analysis as these showed improved data quality. We used a total of 28 individual 2-D lines, most of which ran either North-South or East-West. The seismic lines were visualised using OpendTect (<https://www.dgbes.com>). Large normal faults were typically clearly visible (Figure 6), running from near-surface layers through Mesozoic sediments and to the limits of well-resolved data. These faults were picked on individual lines and then their positions extrapolated between each 2-D line. The spacing of 2-D lines is such that the interpreted fault positions shown in Figure 2 are not unique, but the overall pattern of both northward and southward-dipping, east-west trending normal faults is clear. In total we mapped 14 faults in the area.

S7 Moment tensor dip uncertainty

Although the focal mechanisms for events that occurred before the full installation of the local network have a strike closer to WNW-ESE (Figure 2, Figure 5c), this could reflect the curved strike of the NGF or more likely, could be an artefact due to insufficient station coverage.

We inverted for a moment tensor using a fixed mechanism using the same fault geometry as the best solution for all events but forcing a south-dipping fault. We found that this a south-dipping

fault fails explain the observed waveforms as well, reducing the optimum variance reduction by 36% relative to the best-fitting (north-dipping) moment tensor. Furthermore, we found a small moment tensor uncertainty corresponding to a mean Kagan angle of 5° .

Supplementary Figures

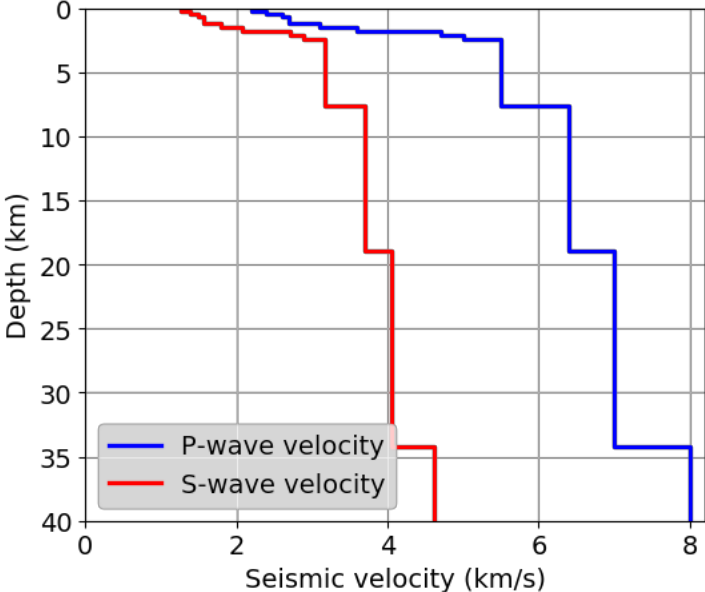


Figure S1: Our optimum 1-D P- and S-wave layered velocity model used for event relocations and moment tensor inversion, which is based on a nearby interpreted well log at the Brockham field.

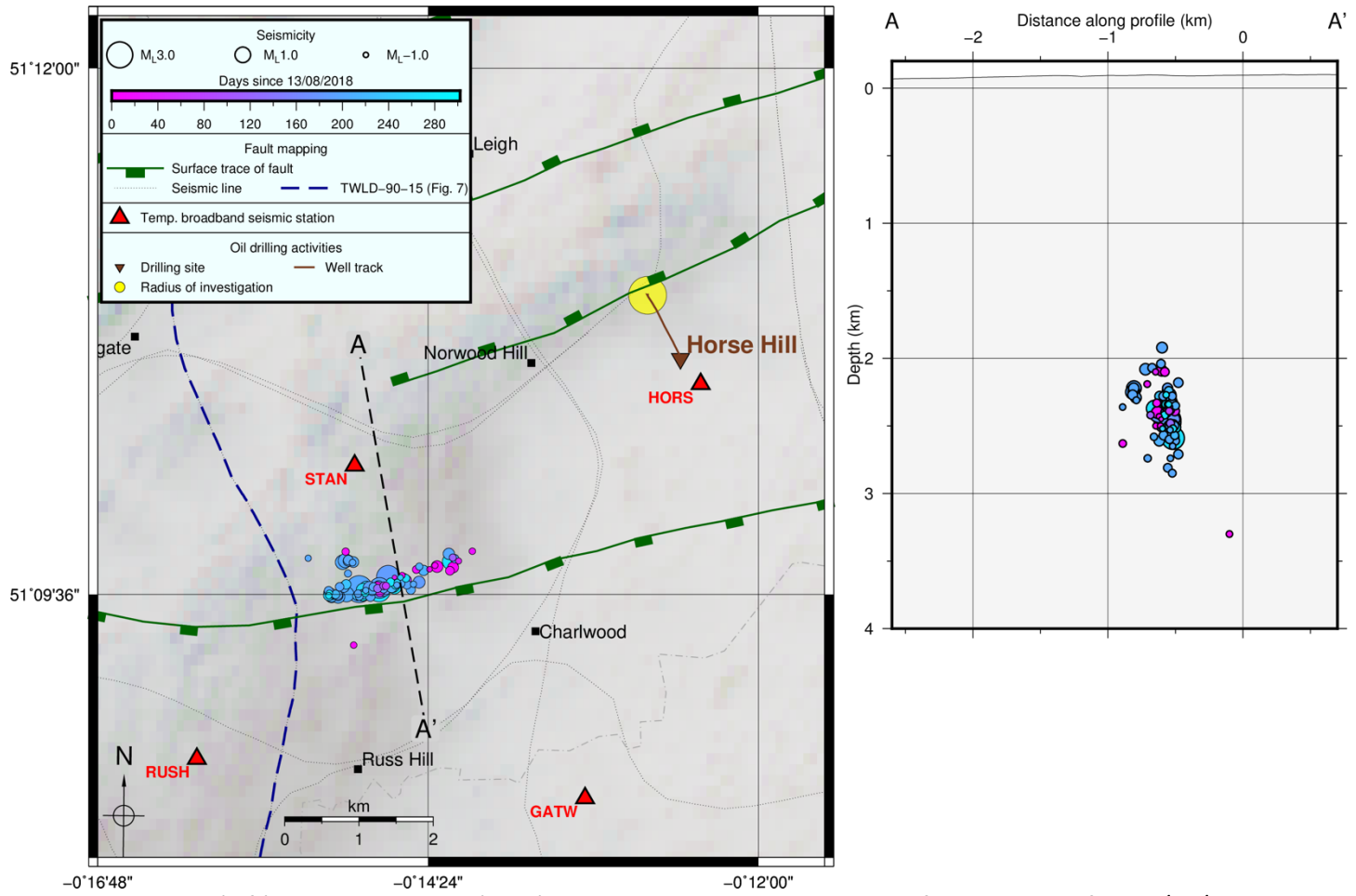


Figure S2: Map (left) and cross-section (right) showing the HypoDD relocations for 89 events after 13/08/2018 and coloured by time.

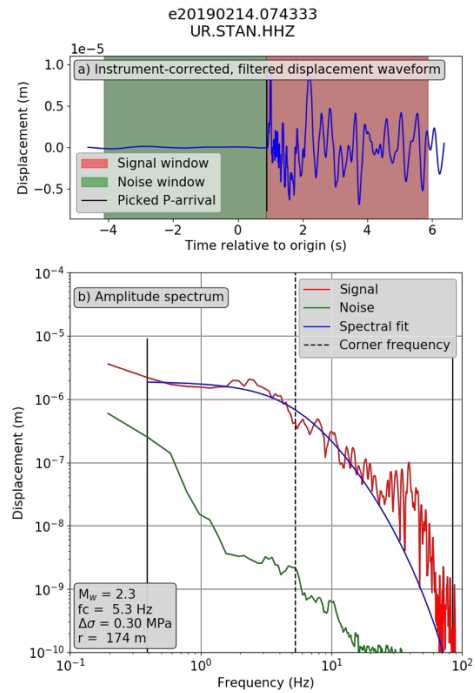
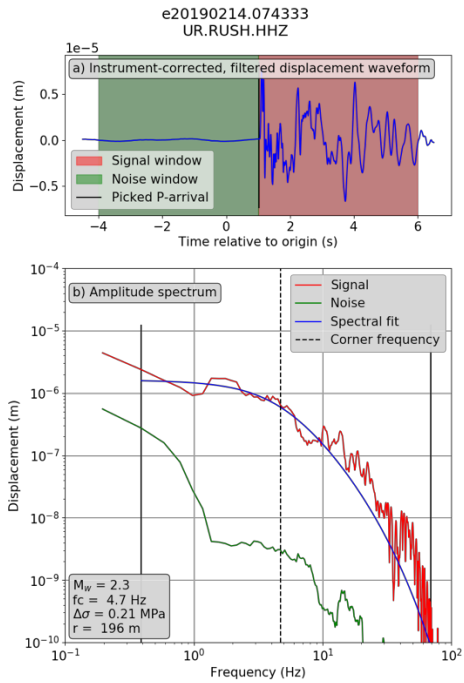
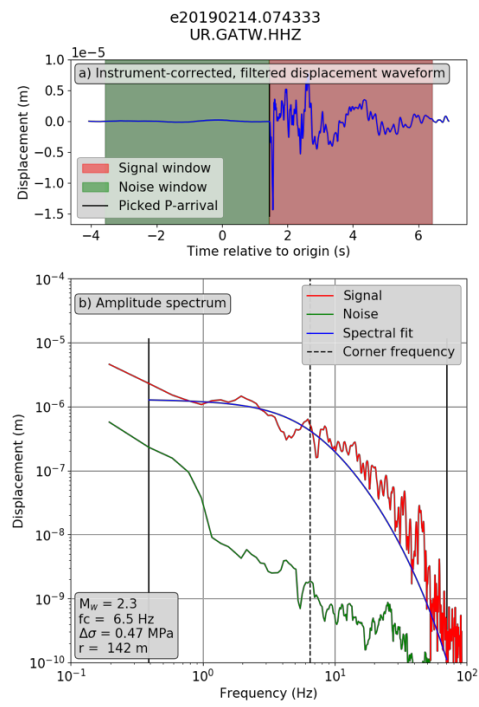
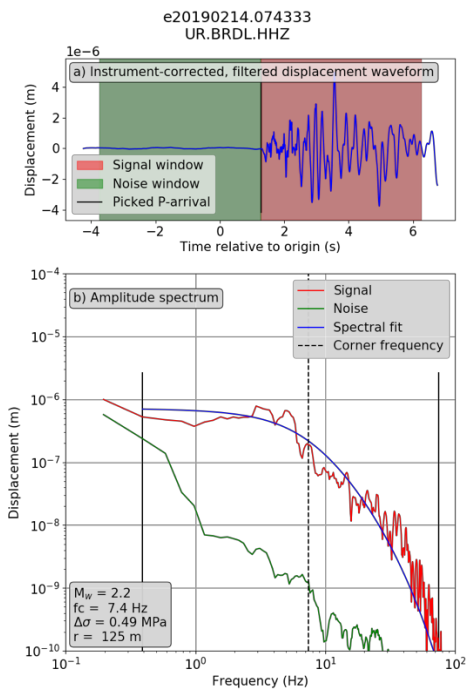


Figure S3: Spectral fits to displacement spectra for the 2017-02-14 event. Each of the four panels shows the waveforms and spectral fits for four of the near-field seismic monitoring stations. Computed source parameters are shown in the white box in each case.

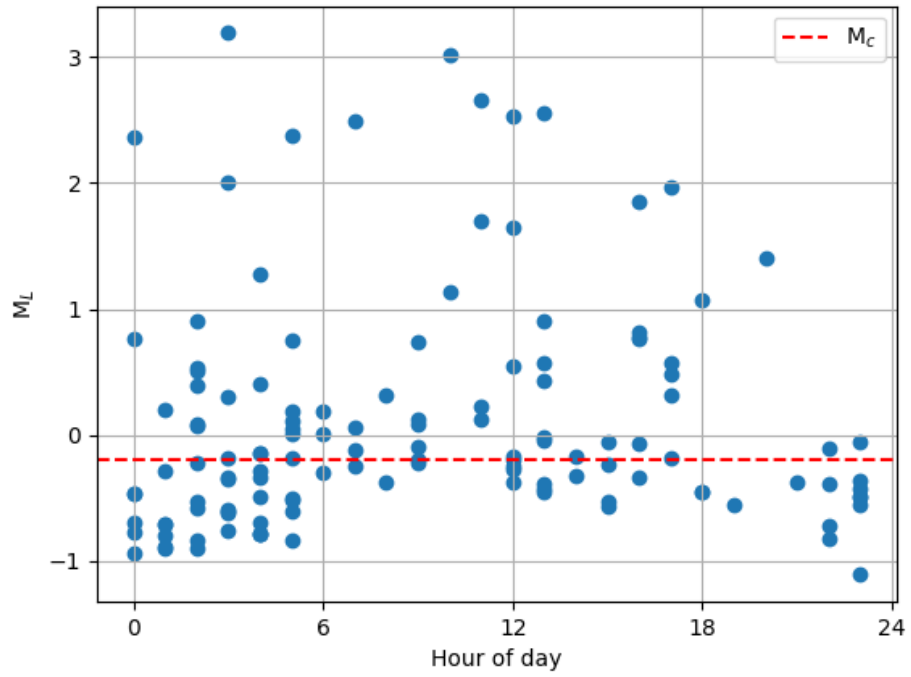


Figure S4: Scatter plot showing local magnitude versus hour of day for all detected events. The red line shows the magnitude of completeness based on analysis of the frequency-magnitude distribution.

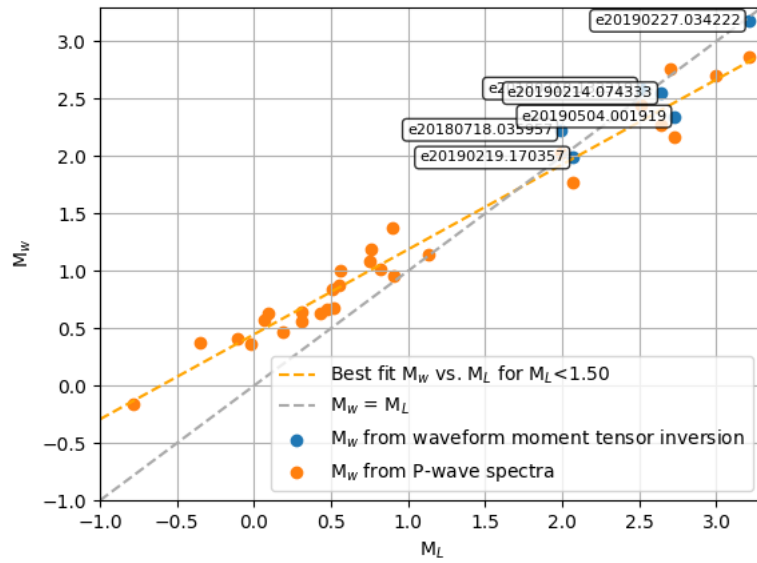


Figure S5: Scaling between local magnitude, M_L with estimated moment magnitude from P-wave spectral inversion and from moment tensor inversion for the larger events (labelled). The orange line shows a regression fit between M_L and M_w calculated from spectra, and this fit is used to compute equivalent moment magnitudes for Gutenberg-Richter analysis in Figure 7b.

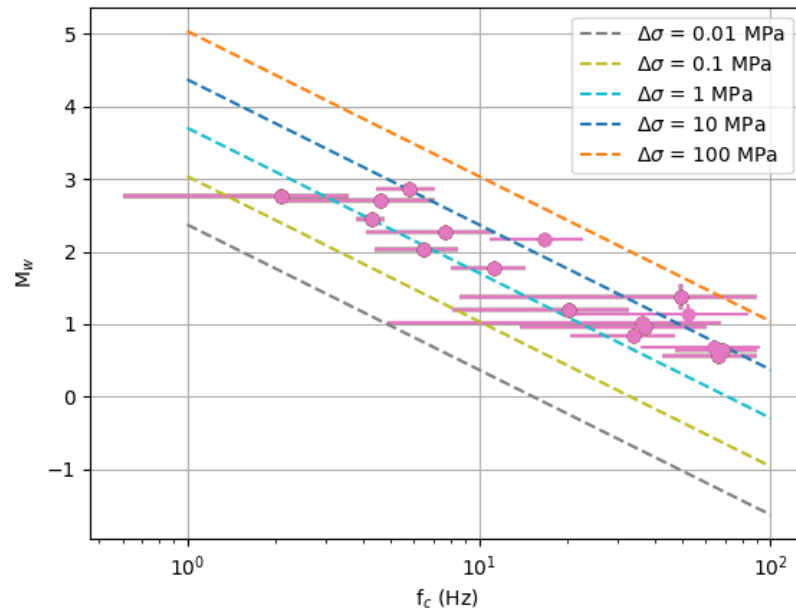


Figure S6: Estimated stress drops for a cluster of 17 events recorded on the local temporary seismic network from P-wave spectra and assuming a Brune source model. Error bars show standard deviations in corner frequency and moment magnitude

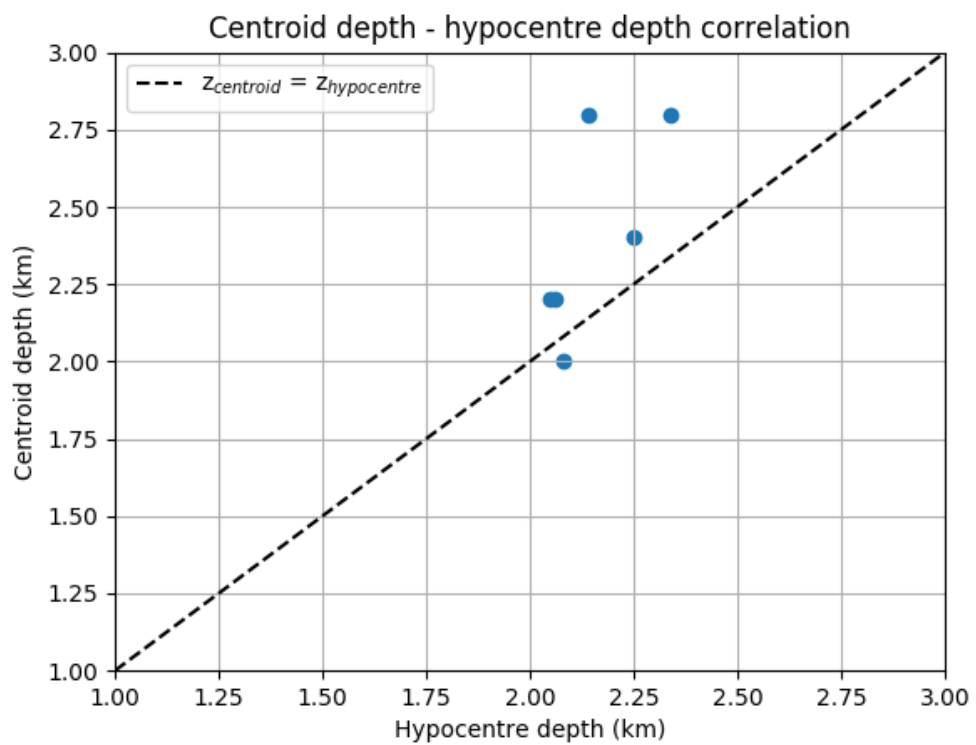


Figure S7: Correlation between magnitude (a) and depth (b) estimates from hypocentre location and moment tensor inversion.

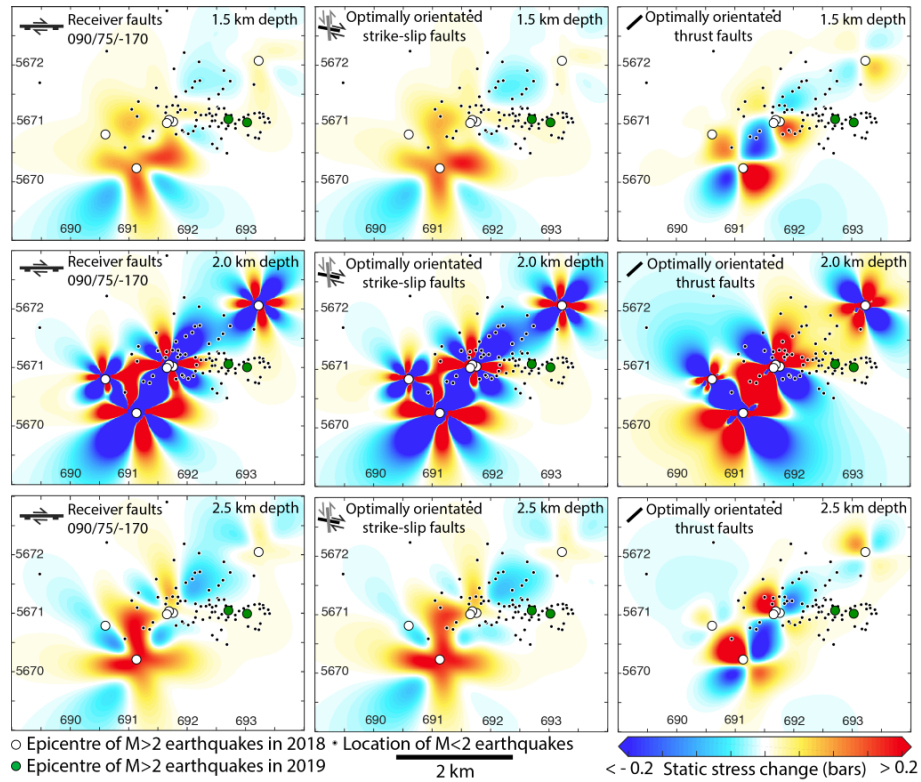


Figure S8: Static stress changes associated with M>2 earthquakes in 2018, resolved onto faults with three different geometries, 1.) parallel to the Newdigate/Horse Hill faults, 2.) optimally orientated strike-slip faults and 3.) optimally orientated thrust faults, at a range of depths. Across the range of uncertainties, the majority of earthquakes in the sequence, including the M>2 events in 2019, plot in regions of positive static stress change, suggesting that static stress triggering has played a role in this sequence.

Supplementary Tables

Table S1: Layered velocity model used for the hypocentre relocation and moment tensor inversion in this study.

Depth to top of layer (km)	P-wave velocity (km/s)	S-wave velocity (km/s)
0.0	2.2	1.3
0.2	2.4	1.4
0.4	2.6	1.5
0.7	2.7	1.6
1.2	3.1	1.8
1.5	3.6	2.1
1.8	4.7	2.7
2.1	5.0	2.9
2.4	5.5	3.2
7.6	6.4	3.7
18.9	7.0	4.1
34.2	8.0	4.6

Table S2: Summary of hypocentre parameters relocated using NonLinLoc. The * symbol denotes a fixed hypocentre depth due to the lack of nearby seismic stations. The † symbol denotes a poorly constrained hypocentre location due to poor azimuthal coverage. For a detailed dataset of source parameters, please see the spreadsheet located at

<https://docs.google.com/spreadsheets/d/1ICrOJtql1syPlofSe00Cp0RJQkO36IBLuy8CrA7EAU/edit?usp=sharing>.

Date	Time (UTC)	Latitude (°)	Longitude (°)	Depth (km)	M_L
01/04/2018	11:10:58	51.1588	-0.2591	2.33*	2.66
01/04/2018	11:14:00	51.1551	-0.2698	2.33*	1.70
01/04/2018	12:11:12	51.1700	-0.2734	2.33*	1.65
09/04/2018	04:13:58	51.1924	-0.2067	2.33*	1.28
28/04/2018	20:38:35	51.1655	-0.2900	2.33*	1.40
27/06/2018	12:28:23	51.1678	-0.2365	2.33*	2.53
29/06/2018	05:54:10	51.1573	-0.2745	2.33*	2.38
05/07/2018	10:53:24	51.1528	-0.2674	2.33*	3.02
10/07/2018	16:03:10	51.1640	-0.2377	2.33*	1.85
17/07/2018	02:24:52	51.1595	-0.2472	1.90	0.39
17/07/2018	02:27:01	51.1588	-0.2448	1.86	-0.53
18/07/2018	03:59:56	51.1588	-0.2579	2.08	2.01
18/07/2018	04:00:09	51.1551	-0.2484	1.80	0.40
18/07/2018	13:33:18	51.1592	-0.2585	2.06	2.55
18/07/2018	13:33:39	51.1573	-0.2555	1.93	0.90
18/07/2018	16:28:28	51.1543	-0.2472	2.16	0.77
22/07/2018	05:11:53	51.1565	-0.2365	0.40	0.05
25/07/2018	18:50:21	51.1610	-0.2591	2.10	1.07
26/07/2018	23:20:13	51.1577	-0.2442	2.62	-0.43
27/07/2018	23:37:05	51.1625	-0.2567	1.13†	-0.56
28/07/2018	05:56:27	51.1562	-0.2394	1.83	-0.51
30/07/2018	11:03:38	51.1375	-0.2287	0.39†	0.12
01/08/2018	01:59:01	51.1595	-0.2507	2.03	-0.29
08/08/2018	04:34:56	51.1588	-0.2519	1.73	-0.49
11/08/2018	15:08:34	51.1597	-0.2487	1.81	-0.53
13/08/2018	13:36:52	51.1564	-0.2635	2.37	0.43
14/08/2018	01:23:24	51.1575	-0.2504	2.35	-0.90
15/08/2018	00:11:06	51.1573	-0.2626	2.31	-0.94
15/08/2018	09:15:06	51.1567	-0.2570	2.63	0.12
15/08/2018	12:28:55	51.1586	-0.2445	2.25	-0.27
17/08/2018	22:07:55	51.1565	-0.2484	2.18	-0.82
18/08/2018	03:21:58	51.1579	-0.2522	2.35	0.30
19/08/2018	22:21:27	51.1586	-0.2481	2.09	-0.72
24/08/2018	02:53:43	51.1595	-0.2496	2.57	-0.83
26/08/2018	15:15:03	51.1573	-0.2424	2.27	-0.57
27/08/2018	06:58:19	51.1567	-0.2540	2.40	-0.30
28/08/2018	16:24:37	51.1565	-0.2650	2.53	-0.34
30/08/2018	00:22:10	51.1579	-0.2487	2.36	-0.47

02/09/2018	01:45:27	51.1571	-0.2552	2.40	-0.71
15/09/2018	01:17:28	51.1536	-0.2448	2.46	-0.80
16/09/2018	23:51:50	51.1577	-0.2466	2.36	-1.11
25/09/2018	05:26:53	51.1594	-0.2433	2.30	-0.18
28/09/2018	22:55:00	51.1781	-0.2260	2.25	-0.11
16/10/2018	19:52:12	51.1590	-0.2451	2.57	-0.56
19/10/2018	23:43:45	51.1758	-0.2582	2.50	-0.36
27/10/2018	15:02:03	51.1586	-0.2475	2.51	-0.06
20/11/2018	00:54:59	51.1582	-0.2457	2.30	-0.46
04/12/2018	05:07:15	51.1571	-0.2528	2.14	-0.60
15/12/2018	18:11:55	51.1595	-0.2448	2.50	-0.45
28/12/2018	17:15:08	51.1623	-0.2671	2.26 [†]	-0.18
02/01/2019	12:02:46	51.1665	-0.2570	3.14	-0.17
10/02/2019	17:10:10	51.1579	-0.2409	2.35	0.31
14/02/2019	07:43:33	51.1586	-0.2439	2.34	2.49
14/02/2019	08:02:53	51.1612	-0.2612	2.05	0.32
16/02/2019	06:58:46	51.1769	-0.2552	2.15	0.19
18/02/2019	13:16:20	51.1577	-0.2418	2.51	-0.04
19/02/2019	02:38:52	51.1678	-0.2531	3.13	-0.90
19/02/2019	17:03:57	51.1616	-0.2564	2.05	1.97
20/02/2019	17:27:36	51.1582	-0.2409	2.43	0.48
23/02/2019	04:43:10	51.1603	-0.2674	2.01	-0.34
26/02/2019	13:27:55	51.1577	-0.2418	2.39	-0.43
27/02/2019	03:42:21	51.1582	-0.2397	2.14	3.19
27/02/2019	03:43:40	51.1640	-0.2531	2.42	-0.34
27/02/2019	03:43:54	51.1580	-0.2400	2.25	-0.18
27/02/2019	03:51:32	51.1642	-0.2427	2.36	-0.35
27/02/2019	03:59:30	51.1646	-0.2499	2.64	-0.60
27/02/2019	04:11:32	51.1655	-0.2507	2.65	-0.79
27/02/2019	04:46:52	51.1556	-0.2374	2.28	-0.15
27/02/2019	05:17:39	51.1620	-0.2469	2.19	-0.50
27/02/2019	07:25:54	51.1573	-0.2448	2.44	-0.25
27/02/2019	08:24:13	51.1640	-0.2567	2.31	-0.37
27/02/2019	09:15:36	51.1603	-0.2388	2.31	0.08
27/02/2019	09:43:16	51.1590	-0.2356	2.30	-0.19
27/02/2019	12:35:22	51.1597	-0.2380	2.22	0.55
27/02/2019	13:05:33	51.1590	-0.2368	2.48	0.57
27/02/2019	13:05:46	51.1586	-0.2350	2.29	-0.02
27/02/2019	15:45:52	51.1620	-0.2433	2.54	-0.24
27/02/2019	16:04:34	51.1580	-0.2353	2.27	-0.07
28/02/2019	03:16:44	51.1678	-0.2496	3.25	-0.59
28/02/2019	04:26:10	51.1556	-0.2380	2.30	-0.69
28/02/2019	04:48:50	51.1612	-0.2582	1.77	-0.78
28/02/2019	05:37:53	51.1564	-0.2385	2.45	0.01
28/02/2019	05:39:37	51.1560	-0.2380	2.30	0.11
28/02/2019	07:07:49	51.1562	-0.2394	2.47	0.06
28/02/2019	09:33:29	51.1640	-0.2603	2.65	-0.10
28/02/2019	11:15:48	51.1597	-0.2665	2.00	0.22
28/02/2019	13:02:12	51.1580	-0.2341	2.25	-0.39
28/02/2019	16:51:59	51.1607	-0.2490	3.11	0.82

28/02/2019	16:52:06	51.1577	-0.2442	2.73	0.76
01/03/2019	00:00:00	51.1579	-0.2439	2.19	-0.77
02/03/2019	09:50:27	51.1603	-0.2531	1.69	-0.22
03/03/2019	02:33:18	51.1594	-0.2391	2.19	0.91
03/03/2019	04:48:14	51.1586	-0.2415	2.22	-0.28
03/03/2019	22:31:33	51.1582	-0.2457	2.33	-0.39
04/03/2019	14:18:06	51.1590	-0.2403	2.16	-0.17
05/03/2019	12:16:45	51.1601	-0.2558	1.70	-0.25
06/03/2019	18:18:56	51.1580	-0.2377	2.05	-0.45
07/03/2019	05:53:38	51.1601	-0.2522	1.57	-0.83
08/03/2019	02:39:41	51.1594	-0.2362	2.31	0.51
08/03/2019	02:40:30	51.1595	-0.2365	2.33	0.07
08/03/2019	03:01:42	51.1605	-0.2600	1.67	-0.62
10/03/2019	06:51:21	51.1663	-0.2472	2.07	0.01
14/03/2019	01:00:58	51.1590	-0.2445	2.29	0.20
21/03/2019	13:08:47	51.1588	-0.2400	2.16	-0.45
22/03/2019	14:02:45	51.1594	-0.2362	2.26	-0.33
26/03/2019	23:04:41	51.1595	-0.2377	2.38	-0.49
28/03/2019	21:07:53	51.1590	-0.2415	2.24	-0.38
30/03/2019	07:20:47	51.1603	-0.2365	2.29	-0.12
05/04/2019	00:58:01	51.1558	-0.2531	1.77	-0.70
11/04/2019	00:18:34	51.1594	-0.2421	2.54	0.76
11/04/2019	01:20:04	51.1579	-0.2463	2.26	-0.89
15/04/2019	23:54:51	51.1601	-0.2368	2.38	-0.05
16/04/2019	01:17:42	51.1577	-0.2490	2.32	-0.71
22/04/2019	17:16:55	51.1594	-0.2415	2.50	0.57
04/05/2019	00:19:19	51.1595	-0.2436	2.25	2.36
04/05/2019	02:03:08	51.1594	-0.2457	2.37	0.53
04/05/2019	23:20:46	51.1586	-0.2487	2.33	-0.49
05/05/2019	02:11:19	51.1594	-0.2457	2.32	-0.22
06/05/2019	02:55:36	51.1601	-0.2374	2.32	0.08
06/05/2019	03:01:11	51.1601	-0.2380	2.33	-0.76
06/05/2019	10:19:23	51.1579	-0.2528	2.29	1.13
07/05/2019	02:04:58	51.1605	-0.2433	2.52	-0.58
07/05/2019	04:05:35	51.1597	-0.2421	2.36	-0.15
07/05/2019	04:21:14	51.1605	-0.2368	2.30	-0.78
09/05/2019	09:46:43	51.1594	-0.2457	2.26	0.74
10/05/2019	12:10:37	51.1579	-0.2457	2.30	-0.38
10/05/2019	12:49:43	51.1666	-0.2109	2.13	-0.20
11/05/2019	05:05:01	51.1601	-0.2421	2.30	0.19
11/05/2019	05:05:37	51.1601	-0.2421	2.22	0.75

Table S3: Static stress transferred to the epicentres of the M>2 earthquakes in the sequence from all prior M>2 earthquakes.

Date and magnitude of earthquake	Static stress at epicentre (bars)	Notes
27/06/18, M _L 2.5	-0.0045	±30° strike makes stress positive
29/06/18, M _L 2.4	0.0109	
05/07/18, M _L 3.0	-0.0626	Difficult to make positive with changes in strike or depth
18/07/18, M _L 2.0	-8.1352	Too close to location of the first earthquake on 01/04/18 to draw conclusion
18/07/18, M _L 2.5	-4.4294	Too close to location of the first earthquake on 01/04/18 to draw conclusion
14/02/19, M _L 2.5	-0.0002	±0.1km change in depth changes stress to positive
27/02/19, M _L 3.1	0.0102	